Transient spectroscopy from time-dependent electronic-structure theory without multipole expansions

Einar Aurbakken,[1,*] Benedicte Sverdrup Ofstad,[1] Håkon Emil Kristiansen,[1] Øyvind Sigmundson Schøyen,[2] Simen Kvaal,[1] Lasse Kragh Sørensen,[3] Roland Lindh,[4] and Thomas Bondo Pedersen[1,†]

[1]*Hylleraas Centre for Quantum Molecular Sciences, Department of Chemistry, University of Oslo, 0371 Oslo, Norway*

[2]*Department of Physics, University of Oslo, 0371 Oslo, Norway*

[3]*University Library, University of Southern Denmark, 5230 Odense M, Denmark*

[4]*Department of Chemistry—BMC, Uppsala University, 75123 Uppsala, Sweden*

(Received 5 July 2023; accepted 22 November 2023; published 22 January 2024)

Based on the work done by an electromagnetic field on an atomic or molecular electronic system, a general gauge-invariant formulation of transient absorption spectroscopy is presented within the semiclassical approximation. Avoiding multipole expansions, a computationally viable expression for the spectral response function is derived from the minimal-coupling Hamiltonian of an electronic system interacting with one or more laser pulses described by a source-free, enveloped electromagnetic vector potential. With a fixed-basis expansion of the electronic wave function, the computational cost of simulations of laser-driven electron dynamics beyond the dipole approximation is the same as simulations adopting the dipole approximation. We illustrate the theory by time-dependent configuration interaction and coupled-cluster simulations of core-level absorption and circular dichroism spectra.

DOI: 10.1103/PhysRevA.109.013109

I. INTRODUCTION

Using technology developed in the past two decades, ultrashort laser pulses with attosecond duration have enabled the observation and manipulation of multielectron dynamics in atoms, molecules, and materials, thus opening new research avenues in physics and chemistry [1–3]. Quantum-mechanical simulations are mandatory to properly understand, interpret, and predict advanced attosecond experiments. While nuclear motion becomes important on longer timescales (femtoseconds), one- and multielectron ionization dynamics constitute major challenges for time-dependent electronic-structure simulations, along with electron-correlation effects [4].

Single-active-electron (SAE) models [5–7] that, at best, only account for electron correlation through an effective potential are widely used to study processes induced by lasers with frequency well below any multielectron excitation energy. As the frequency increases and approaches resonance with a multielectron excited state, the SAE approximation breaks down and a correlated many-body method should be applied instead [8,9].

Regardless of whether the SAE model or a many-body description is used, most simulations of laser-induced processes employ the electric dipole approximation where the magnetic component of the laser field is neglected and the electric component is assumed to be spatially uniform. This is an excellent approximation when the spatial extent of the electronic system is small compared with the wavelength of the laser field. Attosecond laser pulses, however, are commonly generated by high harmonic generation in the extreme ultraviolet and x-ray spectral regions where beyond-dipole effects may become non-negligible. It is therefore of interest to include higher-order electric and magnetic multipole interactions in simulations of laser-driven electron dynamics, preferably without incurring a significant computational penalty.

Within response theory [10], which is essentially time-dependent perturbation theory Fourier transformed to the frequency domain, beyond-dipole effects have been studied using the full plane-wave vector potential for the semiclassical description of the matter-field interaction [11–14]. Due to the use of perturbation theory and the neglect of terms quadratic in the vector potential, these studies are limited to weak laser fields but do not suffer from issues such as origin dependence and slow basis-set convergence that may arise from the use of multipole expansions [15–18]. Conceptually, at least, it is rather straightforward to generalize the response-theory approaches to the time domain, avoiding perturbation theory altogether and hence enabling the study of both weak- and strong-field processes without multipole expansions.

The theory of transient absorption spectroscopy (TAS) (see, e.g., the work by Wu *et al.* [19]) has been formulated in the framework of the electric dipole approximation. In the present work, we present a generalization that accounts for the presence of spatially nonuniform fields, which reduces to the original formulation in the long-wavelength (electric dipole) limit. In line with the previous work based on response theory [11–14], we present initial test simulations on small molecules in the weak-field limit using time-dependent configuration-interaction (TDCI) [20–24] and time-dependent

*einar.aurbakken@kjemi.uio.no

†t.b.pedersen@kjemi.uio.no

coupled-cluster (TDCC) [25] theories. Ignoring ionization processes, we use static, atom-centered Gaussian basis sets such that the prerequisite integrals involving the full plane-wave vector potential can be computed using the recent implementation reported by Sørensen *et al.* [13]. This allows us to validate our implementation of the generalized theory of TAS by comparing with previously reported theoretical pump-probe and x-ray-absorption spectra. In addition, we compute the anisotropic x-ray circular dichroism (CD) spectrum of hydrogen peroxide generated from simulations of the electrons interacting with circularly polarized laser pulses [26–31], comparing with the CD spectrum predicted by the rotatory strength tensor [32].

II. THEORY

Atomic and molecular transient (as well as steady-state) absorption spectra can be obtained by computing the spectral response function $S(\omega)$, which in turn is obtained from a frequency-resolved analysis of the total energy transfer $\Delta\mathcal{E}$ between an electromagnetic field and the electronic system. The spectral response function $S(\omega)$ is defined such that it satisfies the relation

$$\Delta\mathcal{E} = \int_0^\infty \mathrm{d}\omega\, \omega S(\omega). \tag{1}$$

The absorption cross section $\sigma(\omega)$ can be computed as

$$\sigma(\omega) = \frac{\omega S(\omega)}{I(\omega)}, \tag{2}$$

where $I(\omega)$ is the total field energy per unit area at frequency ω. In this work, however, we focus on the spectral response function. We first formulate a general gauge-invariant theory for the energy transfer, proceeding to the derivation of the spectral response function for the specific case of an enveloped, source-free electromagnetic field without multipole expansion.

We will closely follow the theory previously formulated within (and restricted to) the electric dipole approximation [19,33–35]. The key difference between the theory within and without the electric dipole approximation is the definition of the proper gauge-invariant energy transfer $\Delta\mathcal{E}$. Once this has been established, the derivation of the spectral response function $S(\omega)$ proceeds in essentially the same manner within and without the electric dipole approximation.

A. Energy transfer

We consider an atomic or molecular electronic system exposed to the classical electromagnetic fields

$$\boldsymbol{E}(\boldsymbol{r},t) = -\partial_t \boldsymbol{A}(\boldsymbol{r},t) - \nabla\phi(\boldsymbol{r},t), \tag{3}$$

$$\boldsymbol{B}(\boldsymbol{r},t) = \nabla \times \boldsymbol{A}(\boldsymbol{r},t), \tag{4}$$

where $\boldsymbol{A}(\boldsymbol{r},t)$ and $\phi(\boldsymbol{r},t)$ are the vector and scalar potentials, respectively. Specifically, we consider the interactions of the electrons with laser pulses, i.e., the physical electric and magnetic fields $\boldsymbol{E}$ and $\boldsymbol{B}$, respectively, to be nonzero only in a finite time interval and to vanish as $t \to \pm\infty$. Within the nonrelativistic clamped-nuclei Born-Oppenheimer approximation, the time evolution of the electronic system is governed by the electronic Schrödinger equation

$$\mathrm{i}|\dot{\Psi}(t)\rangle = H(t)|\Psi(t)\rangle, \quad |\Psi(t\to-\infty)\rangle = |\Psi_0\rangle, \tag{5}$$

where $|\Psi_0\rangle$ is the initial wave function of the electrons, typically the ground-state wave function in the absence of external fields. The semiclassical minimal-coupling Hamiltonian is given by

$$H(t) = \tfrac{1}{2}\pi^2(\boldsymbol{r},t) + W - \phi(\boldsymbol{r},t), \tag{6}$$

where $\boldsymbol{\pi}(\boldsymbol{r},t) = \boldsymbol{p} + \boldsymbol{A}(\boldsymbol{r},t)$ is the kinetic momentum operator and W represents all Coulomb interactions among the electrons and (clamped) nuclei. Throughout this paper, summation over electrons will be implicitly assumed for brevity of notation, and Hartree atomic units are used. We have also skipped the spin Zeeman term as we will use only closed-shell spin-restricted wave functions in the present work.

We wish to derive a general expression for the spectral response function $S(\omega)$ in Eq. (1). Physically, the total energy transfer $\Delta\mathcal{E}$ expresses the work performed on the electronic system by the external electromagnetic fields, and the rate of change of the energy is referred to as the power. In classical electrodynamics [36], the power function of an electron in an electromagnetic field is given by $P = -\boldsymbol{E}\cdot\boldsymbol{v}$, where $\boldsymbol{v}$ is the velocity of the electron. This is also the energy lost by the electromagnetic field as calculated by Poynting's theorem [36], ensuring energy conservation (of the particle and field systems together). Assuming that the electric field $\boldsymbol{E}(\boldsymbol{r},t)$ is an analytic function of $\boldsymbol{r}$, we show in Appendix A that the quantum-mechanical power operator can be obtained from McCoy's formulation of Weyl quantization as [37,38]

$$P(\boldsymbol{r},t) = -\tfrac{1}{2}[\boldsymbol{E}(\boldsymbol{r},t)\cdot\boldsymbol{\pi}(\boldsymbol{r},t) + \boldsymbol{\pi}(\boldsymbol{r},t)\cdot\boldsymbol{E}(\boldsymbol{r},t)]. \tag{7}$$

Hence, we may express the total energy transferred from the field to the electronic system as

$$\Delta\mathcal{E} = \int_{-\infty}^{\infty} \mathrm{d}t\, \langle P(\boldsymbol{r},t)\rangle. \tag{8}$$

In previous work on transient absorption spectroscopy (see, e.g., Refs. [19,33–35]) the energy transfer is expressed as the integral

$$\Delta\mathcal{E} = \int_{-\infty}^{\infty} \mathrm{d}t\, \frac{\mathrm{d}\mathcal{E}(t)}{\mathrm{d}t}, \tag{9}$$

where $\mathcal{E}(t)$ is the instantaneous energy of the electrons. At this point, the instantaneous energy is typically equated with the quantum-mechanical expectation value of the Hamiltonian $\langle H(t)\rangle = \langle\Psi(t)|H(t)|\Psi(t)\rangle$. In general, however, neither the expectation value $\langle H(t)\rangle$ nor the Hamilton function in classical mechanics [39] equals the energy of the electrons when a time-dependent external electromagnetic field is present. This is clear from the fact that both $\langle H(t)\rangle$ and $\mathrm{d}\langle H(t)\rangle/\mathrm{d}t$ are gauge-dependent quantities. Instead, the operator [40,41]

$$K(t) = H(t) + \phi(\boldsymbol{r},t) = \tfrac{1}{2}\pi^2(\boldsymbol{r},t) + W \tag{10}$$

can be regarded as a (generally time-dependent) energy operator which yields gauge-invariant expansion coefficients and transition probabilities when the wave function is expanded in its (generally time-dependent) eigenstates (see Appendix B

for details). Using the energy operator (10) and the Ehrenfest theorem, we find

$$\frac{\mathrm{d}\mathcal{E}(t)}{\mathrm{d}t} = \frac{\mathrm{d}\langle K(t)\rangle}{\mathrm{d}t} = \langle P(\boldsymbol{r},t)\rangle, \tag{11}$$

which leads to Eq. (8) upon substitution in Eq. (9). We refer the reader to Refs. [40–47] for further discussions of the intricacies of gauge invariance in external time-varying fields.

Within the electric dipole approximation $\boldsymbol{A}(\boldsymbol{r},t) \approx \boldsymbol{A}(\boldsymbol{0},t) = \boldsymbol{A}(t)$, $\phi(\boldsymbol{r},t) = 0$, which was assumed in previous work [19,33–35], the power operator becomes $P(t) = -\boldsymbol{\pi}(t)\cdot\boldsymbol{E}(t)$. Inserting this expression into Eq. (8) yields

$$\Delta\mathcal{E} = -\int_{-\infty}^{\infty} \mathrm{d}t\,\langle\boldsymbol{\pi}(t)\rangle\cdot\boldsymbol{E}(t). \tag{12}$$

Using the Ehrenfest theorem

$$\frac{\mathrm{d}\langle\boldsymbol{r}\rangle}{\mathrm{d}t} = \langle\boldsymbol{\pi}(t)\rangle \tag{13}$$

and integration by parts, we arrive at

$$\Delta\mathcal{E} = \int_{-\infty}^{\infty} \mathrm{d}t\,\langle\boldsymbol{r}\rangle\cdot\dot{\boldsymbol{E}}(t), \tag{14}$$

which agrees with the expressions obtained in Refs. [19,33–35].

Identifying the instantaneous energy as the expectation value $\langle H(t)\rangle$ is valid when the scalar potential vanishes, which in turn is a valid choice with the Coulomb gauge condition $\boldsymbol{\nabla}\cdot\boldsymbol{A}(\boldsymbol{r},t) = 0$ whenever the electric field is divergence-free (no charge contributions to the electric field), i.e., within the radiation gauge [48]. Caused by the absence of magnetic fields, it is a peculiarity of the electric dipole approximation that the correct energy transfer is obtained from $\langle H(t)\rangle$ with the choices $\boldsymbol{A}(\boldsymbol{r},t) = \boldsymbol{0}$ and $\phi(\boldsymbol{r},t) = -\boldsymbol{r}\cdot\boldsymbol{E}(t)$.

B. Representation of laser pulses without multipole expansion

From here on we will assume a divergence-free electric field and work in the radiation gauge such that $K(t) = H(t)$. Following common practice, we separate the Hamiltonian into a time-independent and a time-dependent part

$$H(t) = H_0 + V(t), \tag{15}$$

$$H_0 = \tfrac{1}{2}p^2 + W, \tag{16}$$

$$V(t) = \boldsymbol{A}(\boldsymbol{r},t)\cdot\boldsymbol{p} + \tfrac{1}{2}A^2(\boldsymbol{r},t). \tag{17}$$

In the context of time-dependent perturbation theory or frequency-dependent response theory, the weak-field approximation, i.e., neglecting the term quadratic in the vector potential, is usually invoked, although it is not formally necessary to do so [11–14]. For the real-time simulations pursued in the present work, invoking the weak-field approximation does not lead to any simplifications and hence we retain the quadratic term in all simulations.

The vector potential that solves the Maxwell equations within the Coulomb gauge is a linear combination of plane waves. However, this is impractical for modeling ultrafast laser pulses. We will instead model the vector potential as a linear combination of enveloped plane waves

$$\begin{aligned}\boldsymbol{A}(\boldsymbol{r},t) &= \sum_m \boldsymbol{A}_m(\boldsymbol{r},t)G_m(t)\\ &= \sum_m A_m \mathrm{Re}(\boldsymbol{u}_m \mathrm{e}^{\mathrm{i}(\boldsymbol{k}_m\cdot\boldsymbol{r}-\omega_m t-\gamma_m)})G_m(t),\end{aligned} \tag{18}$$

where each term in the sum models a single pulse with amplitude A_m, carrier frequency ω_m, and carrier-envelope phase γ_m. The Coulomb gauge condition implies that the (complex) polarization vector $\boldsymbol{u}_m$ is orthogonal to the real wave vector $\boldsymbol{k}_m$, which has length ω_m/c, where c is the speed of light. The electric- and magnetic-field amplitudes of each pulse are $E_m = \omega_m A_m$ and $B_m = E_m/c$, respectively, and we define the peak intensity of each pulse as

$$I_m = \tfrac{1}{2}\epsilon_0 c E_m^2. \tag{19}$$

Chirped laser pulses can be modeled by letting γ_m be time dependent.

In experimental work, Gaussian functions are often favored for the envelopes $G_m(t)$. In numerical studies, however, Gaussians are inconvenient due to their long tails and infinite support. For this reason, we use trigonometric envelopes of the form [49]

$$G_m(t) = \begin{cases} \cos^n\left(\frac{\pi(t-t_m)}{T_{mn}}\right), & |t-t_m| \leqslant \frac{T_{mn}}{2} \\ 0, & |t-t_m| > \frac{T_{mn}}{2}, \end{cases} \tag{20}$$

where $n > 0$ is a chosen parameter, t_m is the central time of pulse m, and T_{mn} is the total duration of $\boldsymbol{A}_m$. The total duration depends on n and may be computed from

$$T_{mn} = \frac{\pi\tau_m}{2\arccos(2^{-1/2n})}, \tag{21}$$

where τ_m is the full width at half maximum of $G_m^2(t)$, i.e., τ_m is approximately the desired experimental pulse duration defined from the intensity distribution [49].

The trigonometric envelopes (20) define a sequence of functions that rapidly and uniformly converges to the Gaussian function $\exp[-2\ln(2)(t-t_m)^2/\tau_m^2]$ for increasing values of n [49]. Moreover, in contrast to finite numerical representations of Gaussian envelopes, the trigonometric envelopes guarantee that the dc (zero-frequency) component of the electric field vanishes identically for any choice of $n > 0$, in agreement with the far-field approximation of the Maxwell equations [50].

A similar setup has been used before in grid treatments of single-electron systems [51–53] where pulses of the form

$$\boldsymbol{A}(\boldsymbol{r},t) = A_0 \sin^2\left(\frac{\pi(\omega t - \boldsymbol{k}\cdot\boldsymbol{r})}{\omega T}\right)\sin(\omega t - \boldsymbol{k}\cdot\boldsymbol{r})\boldsymbol{u} \tag{22}$$

were used. Here $\boldsymbol{u}$ is a real polarization vector and the envelope depends *both* on time and on spatial coordinates. This has the benefit of modeling the overall shape of the pulse in space, albeit with potential edge effects if the approximation $\boldsymbol{A}(\boldsymbol{r},t) \approx 0$ at $t = 0$ and $t = T$ is made along with a neglect of the spatial nonperiodicity. The pulse with the purely time-dependent envelope, Eq. (20) with $n = 2$, may be regained from the spatiotemporal envelope by an expansion through lowest order in $\boldsymbol{k}\cdot\boldsymbol{r}/n_{\mathrm{cyc}}$, where n_{cyc} is the number of optical cycles of the pulse.

C. Spectral response function

Since we have assumed a divergence-free electric field, the power operator becomes $P(\boldsymbol{r},t) = -\boldsymbol{E}(\boldsymbol{r},t)\cdot\boldsymbol{\pi}(\boldsymbol{r},t)$, and Eq. (8) simplifies to

$$\Delta\mathcal{E} = -\int_{-\infty}^{\infty} \mathrm{d}t\,\langle \boldsymbol{E}(\boldsymbol{r},t)\cdot\boldsymbol{\pi}(\boldsymbol{r},t)\rangle. \tag{23}$$

Using the Fourier transform convention

$$f(t) = \mathcal{F}_\omega[\tilde{f}(\omega)] = \frac{1}{\sqrt{2\pi}}\int_{-\infty}^{\infty} \mathrm{d}\omega\,\tilde{f}(\omega)e^{\mathrm{i}\omega t}, \tag{24}$$

$$\tilde{f}(\omega) = \mathcal{F}_t[f(t)] = \frac{1}{\sqrt{2\pi}}\int_{-\infty}^{\infty} \mathrm{d}t\,f(t)e^{-\mathrm{i}\omega t}, \tag{25}$$

the integration over time in Eq. (23) can be turned into an integration over frequency,

$$\Delta\mathcal{E} = \int_{-\infty}^{\infty} \mathrm{d}\omega\,Y(\omega), \tag{26}$$

with

$$Y(\omega) = -\mathcal{F}_t[\mathrm{i}\omega\langle\tilde{\boldsymbol{A}}(\boldsymbol{r},\omega)^*\cdot\boldsymbol{\pi}(\boldsymbol{r},t)\rangle], \tag{27}$$

where we have used $\tilde{\boldsymbol{E}}(\boldsymbol{r},\omega)^* = \mathrm{i}\omega\tilde{\boldsymbol{A}}(\boldsymbol{r},\omega)^*$.

Introducing

$$f_{1,m}(\boldsymbol{r}) = \cos(\boldsymbol{k}_m\cdot\boldsymbol{r}), \tag{28}$$

$$f_{2,m}(\boldsymbol{r}) = \sin(\boldsymbol{k}_m\cdot\boldsymbol{r}), \tag{29}$$

$$g_{1,m}(t) = \cos(\omega_m t+\gamma_m)G_m(t), \tag{30}$$

$$g_{2,m}(t) = \sin(\omega_m t+\gamma_m)G_m(t), \tag{31}$$

$$\boldsymbol{u}_m^{ij} = \delta_{ij}\mathrm{Re}(\boldsymbol{u}_m) + \epsilon_{ij}\mathrm{Im}(\boldsymbol{u}_m), \tag{32}$$

where δ_{ij} is the Kronecker delta and ϵ_{ij} is the Levi-Cività symbol, the vector potential (18) can be recast as

$$\boldsymbol{A}_m(\boldsymbol{r},t)G_m(t) = A_m\sum_{i,j=1}^{2}\boldsymbol{u}_m^{ij}f_{i,m}(\boldsymbol{r})g_{j,m}(t). \tag{33}$$

Equation (27) can now be written as

$$Y(\omega) = \omega\sum_m\sum_{i,j=1}^{2}\tilde{F}_{ij,m}(\omega)\tilde{g}_{j,m}(-\omega), \tag{34}$$

where $\tilde{F}_{ij,m}(\omega)$ is the Fourier transform of the function

$$F_{ij,m}(t) = -\mathrm{i}A_m\boldsymbol{u}_m^{ij}\cdot\left(\langle f_{i,m}(\boldsymbol{r})\boldsymbol{p}\rangle + \sum_n\sum_{k,l=1}^{2}A_n\boldsymbol{u}_n^{kl} \times\langle f_{k,n}(\boldsymbol{r})f_{i,m}(\boldsymbol{r})\rangle g_{l,n}(t)\right). \tag{35}$$

Hence,

$$\Delta\mathcal{E} = \int_0^{\infty}\mathrm{d}\omega\,\omega\sum_m\sum_{i,j=1}^{2}[(1-\mathcal{P})\tilde{F}_{ij,m}(\omega)\tilde{g}_{j,m}(-\omega)], \tag{36}$$

where $\mathcal{P}$ is the parity operator defined by $\mathcal{P}f(\omega) = f(-\omega)$. The spectral response function thus becomes

$$S(\omega) = \sum_m\sum_{ij=1}^{2}(1-\mathcal{P})\tilde{F}_{ij,m}(\omega)\tilde{g}_{j,m}(-\omega), \tag{37}$$

which can be computed by sampling $F_{ij,m}(t)$ during a simulation, followed by Fourier transformation in a postprocessing step.

In the electric dipole approximation, $f_{1,m}(\boldsymbol{r}) = 1$ and $f_{2,m}(\boldsymbol{r}) = 0$, and in this case the spectral response function reduces to

$$S(\omega) = 2\,\mathrm{Im}[\langle\tilde{\boldsymbol{\pi}}\rangle(\omega)\cdot\tilde{\boldsymbol{A}}(\omega)^*] \tag{38}$$

or, equivalently,

$$S(\omega) = -2\,\mathrm{Im}[\langle\tilde{\boldsymbol{d}}\rangle(\omega)\cdot\tilde{\boldsymbol{E}}(\omega)^*], \tag{39}$$

in terms of the dipole operator $\boldsymbol{d} = -\boldsymbol{r}$. The expression (39) was used in Refs. [19,33–35]. We remark that Eqs. (38) and (39) are equivalent only if the Ehrenfest theorem (13) is satisfied, i.e., for fully variational many-body wave-function approximations, and in the limit of complete one-electron basis set. For the visual presentation of spectra we use normalized spectral response functions

$$\bar{S}(\omega) = \frac{S(\omega)}{\max[S_{\mathrm{ref}}(\omega)]}, \tag{40}$$

where S_{ref} is the spectral response function of some reference system.

III. NUMERICAL EXPERIMENTS

In order to test the multipole-expansion-free theory outlined above, we will investigate the following aspects: (i) reproducibility of results obtained within the electric dipole approximation in the long-wavelength limit, i.e., the core-level pump-probe spectrum of LiH (Sec. III B); (ii) reproducibility of results obtained with low-order multipole expansions for short wavelengths, i.e., K–pre-edge quadrupole transitions in Ti (Sec. III C); and (iii) intrinsically beyond-dipole phenomena, i.e., anisotropic circular dichroism (Sec. III D).

A. Computational details

All simulations are performed with the open-source software Hylleraas Quantum Dynamics (HYQD) [54]. We employ a series of nonrelativistic, closed-shell, spin-restricted time-dependent electronic-structure methods based on a single reference Slater determinant built from spin orbitals expanded in a fixed atom-centered Gaussian basis set. The orbital expansion coefficients are either kept constant (static orbitals) at the ground-state Hartree-Fock (HF) level or allowed to vary in response to the external field (dynamic orbitals). Static orbitals are used in the time-dependent configuration-interaction singles (TDCIS) [55], time-dependent second-order approximate coupled-cluster singles and doubles (TDCC2) [56,57], and time-dependent coupled-cluster singles and doubles (TDCCSD) [58] methods. Dynamic orbitals are used in the time-dependent Hartree-Fock (TDHF) [55], time-dependent

orbital-optimized second-order Møller-Plesset (TDOMP2) [57,59], and orbital-adaptive time-dependent coupled-cluster doubles (OATDCCD) [60] methods. Only the methods using dynamic orbitals are gauge invariant (in the limit of complete basis set) [61–64]. No splitting of the orbital space is used in the OATDCCD method, which therefore is identical to the nonorthogonal orbital-optimized coupled-cluster doubles model [64]. In the TDHF and TDOMP2 models the dynamic-orbital evolution is constrained to maintain orthonormality throughout, whereas in OATDCCD theory the dynamic orbitals are biorthonormal [60,64].

The methods can be roughly divided into three approximation levels. The TDCIS and TDHF methods are the least computationally demanding ones [with formal scaling $O(K^4)$, with K the number of basis functions] and do not account for electron correlation. The TDCCSD and OATDCCD methods are the most accurate and most expensive [$O(K^6)$] methods with full treatment of double excitations. Finally, the TDCC2 and TDOMP2 methods are intermediate in both accuracy and computational cost [$O(K^5)$]. The TDCC2 method is a second-order approximation to the TDCCSD model, while the TDOMP2 model is the analogous second-order approximation to the orbital-optimized coupled-cluster doubles model [63,65]. The doubles treatment of TDOMP2 theory is essentially identical to that of TDCC2 theory but provides full orbital relaxation through unitary orbital rotations instead of the singles excitations of static-orbital coupled-cluster theory.

Since fixed, atom-centered Gaussian basis sets are used, ionization cannot be described and therefore the simulations are restricted to weak electromagnetic field strengths. On the other hand, the fixed basis set allows us to compute matrix elements of the plane-wave interaction operators using the OPENMOLCAS software package [66,67] via a PYTHON interface implemented in the DALTON PROJECT [68]. The remainder of the Hamiltonian matrix elements and the ground-state HF orbitals are computed using the PYSCF program [69] with the exception of the LiH system, for which the DALTON quantum chemistry package [70] is used. The convergence tolerance for the HF ground states is set to 10^{-10} a.u. for both the HF energy and the norm of the orbital gradients in the PYSCF calculations, while the default value of 10^{-6} a.u. on the HF energy is used in the DALTON calculations. The basis sets are obtained from the PYTHON library BASIS SET EXCHANGE [71]. The systems are initially in the ground state, which is calculated with ground-state solvers implemented in HYQD for all the methods except the TDHF and TDCIS models, for which the ground-state wave function is computed using PYSCF. A convergence tolerance of 10^{-10} is also used for the amplitude residuals in the ground-state coupled-cluster calculations.

The integration of the equations of motion is done with the symplectic Gauss-Legendre integrator [58,72] of order 6 and with a convergence threshold on the residual norm of 10^{-10} for the implicit equations. The simulations are performed with the pulse defined in Eq. (18). The laser pulse parameters will be given for each system below.

In actual simulations, time-dependent functions such as $F_{ij,m}(t)$ and $g_{i,m}(t)$ are computed as discrete time series, forcing us to use the fast Fourier transform algorithm. To reduce the appearance of broad oscillations around the peaks due to spectral leakage, we roughly follow the procedure used by Skeidsvoll *et al.* [34]. The simulation is started at time $t < 0$ when the first pulse is switched on and continued until time $t_{\max} > 0$ after the last pulse is switched off. We then extend the recorded time series such that $t_{\min} = -t_{\max}$ to obtain a symmetric time range about $t = 0$. To do so, we use that $\boldsymbol{A}(\boldsymbol{r}, t) = \boldsymbol{0}$ and hence $V(t) = 0$ in the time interval before the pulse is switched on. We then multiply the resulting time series defined on the uniformly discretized time interval from $t_{\min}$ to $t_{\max}$ with the Hann function

$$w_H(t) = \cos^2\left(\frac{\pi t}{2t_{\max}}\right) \tag{41}$$

before the fast Fourier transform is performed.

B. Core-level pump-probe spectrum of LiH

The most common experimental methods for spectral analysis of attosecond interactions employ pump-probe setups. Therefore, we start by simulating a pump-probe spectrum for LiH. The K–pre-edge features of Li are expected at less than 60 eV, corresponding to a wavelength of approximately 200 Å. In the weak-field limit, the beyond-dipole effects are expected to be quite small, allowing us to compare with the TDCCSD simulations carried out within the electric dipole approximation by Skeidsvoll *et al.* [34].

For the most part we follow the setup of Skeidsvoll *et al.* [34]. We start the TDCCSD simulation at $t = -200$ a.u. and end it at $t_{\max} = 5000$ a.u. The pump pulse centered at $t_1 = -40$ a.u. has a carrier frequency of 3.552 47 eV and maximum electric-field strength of 0.01 a.u. (corresponding to a peak intensity of 3.51×10^{12} W/cm^2), while the probe pulse centered at $t_2 = 0$ a.u. has a carrier frequency of 57.6527 eV and maximum electric-field strength of 0.1 a.u. (peak intensity 3.51×10^{14} W/cm^2). Both pulses are linearly polarized in the z direction (parallel to the molecular axis) with zero carrier-envelope phases, and the propagation direction is along the x axis. The beyond-dipole spectrum is generated using Eq. (37), while Eq. (38) is used to generate the dipole spectrum. The dipole simulation is done in velocity gauge to eliminate any gauge differences between the two simulations. We note in passing that the intensity of the probe pulse is too strong to warrant the complete neglect of ionization processes, but to facilitate comparison with the spectra reported in Ref. [34] we choose to keep it.

Skeidsvoll *et al.* used a Gaussian envelope on the electric field with root-mean-square width $\sigma_1 = 20$ a.u. for the pump pulse and $\sigma_2 = 10$ a.u. for the probe pulse. Here we instead use the trigonometric approximation in Eq. (20) placed on the vector potential with

$$T_{mn} = \frac{\pi\sqrt{\ln(2)}\sigma_m}{\arccos(2^{-1/2n})}, \quad m = 1, 2, \tag{42}$$

and $n = 19$, which is the largest integer for which the pump pulse is strictly zero at $t = -200$ a.u.

There are mainly three aspects of our simulations that will make our dipole spectrum different from that in Ref. [34]: (i) placement of a trigonometric envelope on the vector potential rather than a Gaussian envelope on the electric field, (ii) simulating in the velocity gauge instead of the length gauge, and (iii) using Eq. (38) rather than Eq. (39) to generate the

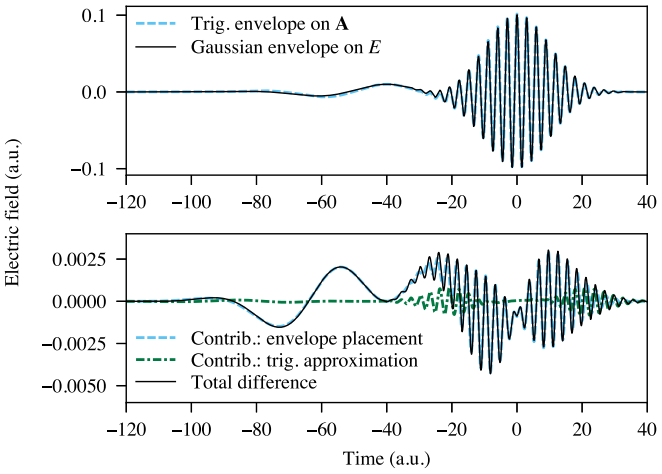

FIG. 1. Shown on top is an electric field with a Gaussian envelope on the electric field and a trigonometric envelope on the vector potential with exponent $n = 19$. On the bottom is the difference between the two pulses and contributions to it from two distinct sources.

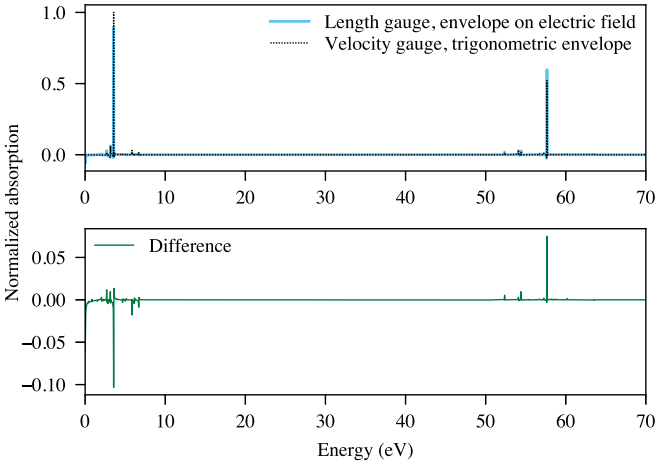

FIG. 2. Shown on top are the TDCCSD pump-probe spectra computed in the electric dipole approximation in length gauge using the Gaussian envelope placed on the electric field and in the velocity gauge with the trigonometric envelope ($n = 19$) on the vector potential. On the bottom is the difference between the solid and dashed lines.

spectra. The first point corresponds to effectively a different electric-field component of the physical pulse, as discussed in more detail in Appendix D. This difference will diminish with increasing number of cycles in the pulses. Both points (ii) and (iii) are due to lacking gauge invariance. Illustrating the difference between the two pulse setups, Fig. 1 shows the z component of the electric field at the origin, $E_z(\mathbf{0}, t)$, with the Gaussian envelope on the electric field and the trigonometric envelope on the vector potential. The bottom panel shows the difference between the two pulse setups, and the contribution to the difference due to the trigonometric approximation and due the placement of the envelope on the vector potential rather than on the electric field. We see that the placement of the envelope is the dominant contribution, especially in the pump region. The difference in the pump region is also more significant due to the smaller amplitude and consequently larger relative difference. Figure 2 shows the TDCCSD dipole spectra generated with the two alternative setups. The length-gauge spectrum is identical to that reported by Skeidsvoll *et al.* [34], and although differences are visible on the scale of the plot, we conclude that the velocity-gauge spectrum conveys the same physics.

Acknowledging the differences between the two setups, we will now focus on the difference between the simulations with and without the dipole approximation. Figure 3 compares the pump-probe spectrum simulated in the dipole approximation and with a plane-wave operator generated with Eqs. (38) and (37), respectively. Evidently, beyond-dipole effects are utterly negligible in this case: The simulation with the plane-wave operator produces a spectrum with the same transition frequencies as the velocity-gauge electric dipole simulations, deviating by at most 4.5×10^{-5}, corresponding to 0.0087%, in relative intensity.

C. *K*–pre-edge quadrupole transitions in Ti

For heavier elements, the bound core-valence excitations move up in energy and the shorter wavelengths become comparable to the "size" of the atoms in terms of, e.g., covalent atomic radii. This implies that higher-order multipole effects become visible in high-resolution spectra. The K edge of Ti is expected at just below 5000 eV. This corresponds to a wavelength of roughly 2.5 Å, which is comparable to the covalent radius of Ti (1.60 Å [73]). Consequently, one can expect visible beyond-dipole effects even in the low-intensity limit.

We consider the Ti^{4+} ion and the $TiCl_4$ molecule. In the Ti^{4+} ion the $1s \rightarrow 3d$ transition is dipole forbidden but quadrupole allowed. In $TiCl_4$ the tetrahedral symmetry splits the $3d$ orbitals into groups of two e orbitals and three t_2 orbitals. The $1s \rightarrow e$ transition is dipole forbidden but quadrupole allowed, while the $1s \rightarrow t_2$ transition attains a

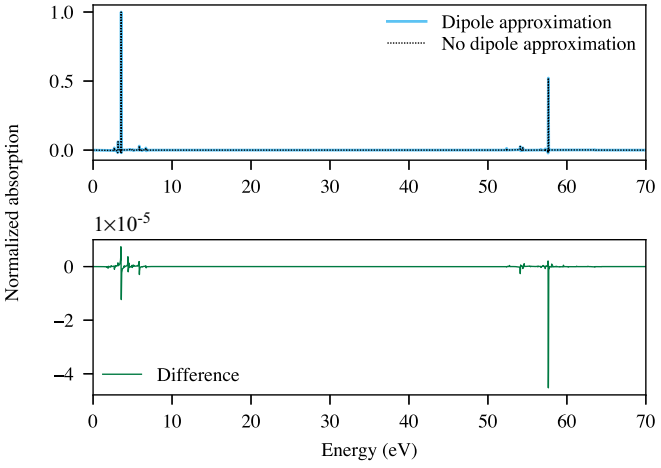

FIG. 3. Shown on top is the pump-probe spectrum of LiH using the TDCCSD method in the dipole approximation and with a plane-wave operator using the aug-cc-pCVDZ basis set. On the bottom is the difference between the spectra generated from simulations in the dipole approximation and with the plane-wave operator.

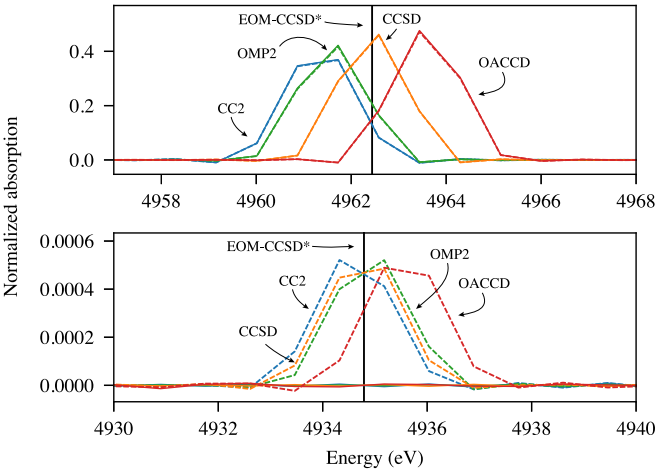

FIG. 4. Plot of the Ti^{4+} K–pre-edge spectrum obtained from simulations with the ANO-RCC-VDZ basis set. Solid lines are obtained with the velocity-gauge electric dipole approximation, while dashed lines are obtained with the plane-wave operator. Shown on top is the dipole-allowed $1s \rightarrow 4p$ transition and on the bottom the quadrupole-allowed $1s \rightarrow 3d$ transition. Vertical black lines indicate the EOMCCSD frequencies reported by Park *et al.* [75]. Note that, although difficult to see, the dashed lines are present also in the top panel

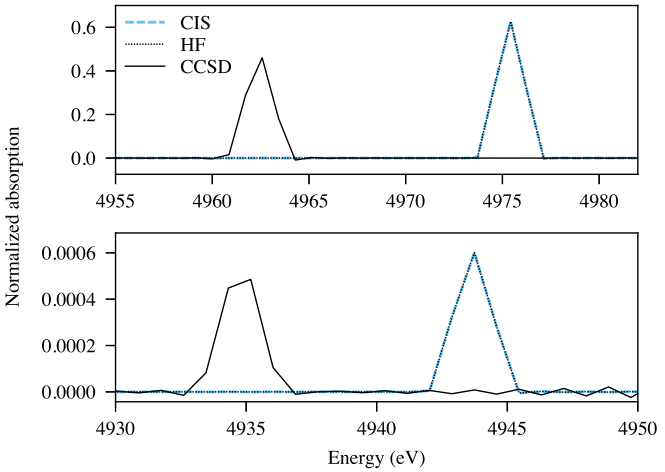

FIG. 5. Plot of the Ti^{4+} K–pre-edge spectrum obtained from simulations with the plane-wave operator. Shown on top is the dipole-allowed $1s \rightarrow 4p$ transition and on the bottom the quadrupole-allowed $1s \rightarrow 3d$ transition.

dominant electric dipole contribution due to $4p$-$3d$ mixing. Experimentally [74], a broad peak around 4969 eV in the x-ray-absorption spectrum of $TiCl_4$ has been assigned to the $1s \rightarrow t_2$ and $1s \rightarrow e$ transitions with most of the intensity stemming from the former. In the implementation presented in this paper, electric quadrupole and other higher-order contributions from the electromagnetic field should automatically be accounted for.

For both the Ti^{4+} and $TiCl_4$ systems, we perform simulations with a ten-cycle pulse with $n = 2$ for the envelope (20), carrier frequency 181 a.u. (4925.26 eV), and carrier-envelope phase $\gamma = 0$. The duration of the simulation is 100 a.u. for Ti^{4+}, while for $TiCl_4$ we use a total simulation time of 600 a.u. to ensure a reasonable resolution of the splitting of the d orbitals. The electric-field strength is $E_1 = 0.01$ a.u. (peak intensity 3.51×10^{12} W/cm^2) and the time step $\Delta t = 2.5 \times 10^{-4}$ a.u. Linearly polarized along the x axis, the pulse is propagated along the z axis (parallel to one of the four Ti-Cl bonds in the case of $TiCl_4$). All Ti^{4+} spectra are normalized relative to the maximum peak in the TDCCSD spectrum.

We first consider the $1s \rightarrow 4p$ and $1s \rightarrow 3d$ transitions of Ti^{4+}, which were studied recently at the equation-of-motion coupled-cluster singles and doubles (EOMCCSD) level of theory by Park *et al.* [75] using multipole expansion up to electric octupole or magnetic quadrupole terms, for the full second-order contribution in the "mixed" length and velocity gauge [17,76,77], in the framework of the Fermi golden rule. In order to compare with their results, we use the ANO-RCC-VDZ basis set [78]. Figure 4 displays the K–pre-edge spectrum obtained for Ti^{4+} with the TDCC2, TDOMP2, TDCCSD, and OATDCCD methods, showing also the transition frequencies obtained by Park *et al.* [75]. To within the spectral resolution of the simulation, the TDCCSD method predicts the same transition frequencies as the static EOMCCSD method, as expected. The intensity of the dipole-allowed $1s \rightarrow 4p$ transition is very nearly the same both with and without the dipole approximation. The orbital-adaptive methods yield roughly the same intensity profiles as their static-orbital counterparts, but the transition frequencies are blueshifted: approximately 0.5 eV for TDOMP2 versus TDCC2 and approximately 2 eV for OATDCCD versus TDCCSD. As has been observed previously [57], these blueshifts are insignificant compared with other sources of error such as basis-set incompleteness and higher-order correlation effects. Electron-correlation effects are significantly more important than the orbital relaxation provided by dynamic orbitals, as seen in Fig. 5, where the TDCCSD spectrum is compared to the spectra obtained with the TDHF and TDCIS methods. While the TDHF and TDCIS simulations produce virtually identical spectra, electron correlation causes a redshift of the transition frequencies by roughly 8 eV. The TDHF and TDCIS intensities are comparable to but slightly higher than the TDCCSD ones. The main source of error, besides relativistic effects, is the choice of basis set: Changing from the ANO-RCC-VDZ basis set to the cc-pVTZ basis set increases the EOMCCSD transition frequencies by more than 28 eV [75]. Since we are not aiming at prediction or interpretation of experimental results in this work, we study the $TiCl_4$ K–pre-edge spectrum using the most affordable TDCIS method with the ANO-RCC-VDZ basis set. The TDCIS spectrum is shown in Fig. 6. The dipole-forbidden $1s \rightarrow e$ transition is visible at 4941.50 eV, roughly 1.5 eV below the dipole-allowed $1s \rightarrow t_2$ transition at 4942.99 eV. The TDCIS frequencies are blueshifted by approximately 12 eV relative to the EOMCCSD results reported by Park *et al.* [75]. The $1s \rightarrow t_2$ transition has a slightly higher intensity with the plane-wave interaction operator than with the dipole interaction operator. It should also be noted, however, that the intensities of the dipole-allowed transitions typically are slightly higher with the dipole approximation and therefore one should be careful using the dipole result as a reference for evaluating the

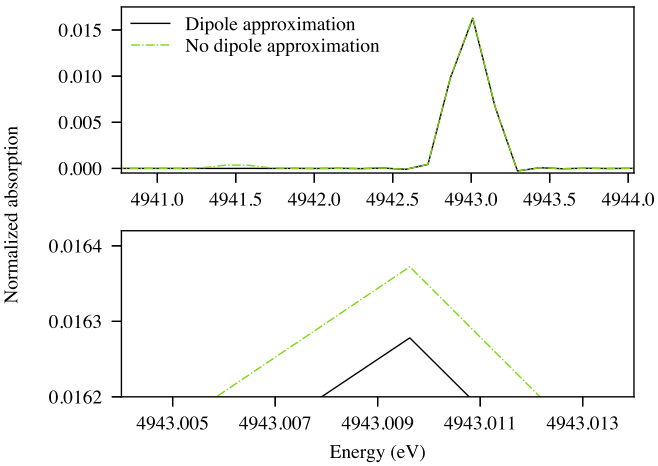

FIG. 6. Plot of the $TiCl_4$ K–pre-edge spectrum from a TDCIS simulation with the plane-wave operator and with the velocity-gauge electric dipole approximation. Shown on top is the dipole-forbidden $1s \rightarrow e$ transition at 4941.50 eV and the $1s \rightarrow t_2$ transition at 4942.99 eV. On the bottom is a close-up at the $1s \rightarrow t_2$ peak.

quadrupole contribution. The deviation may be caused by a difference in the quality of the operator representation or the wave function, which may occur when propagating with different operators in a finite basis set.

D. Anisotropic circular dichroism

Circular dichroism (CD), the difference in absorption of left and right circularly polarized radiation exhibited by chiral molecules, is a particularly interesting case to test the implementation of the beyond-dipole interaction, since the observed effect cannot be explained within the electric dipole approximation. At least electric quadrupole and magnetic dipole terms must be included [79–82] and consequently the differential absorption is weak compared with linear electric dipole absorption. Chiroptical spectroscopies, including CD, are important for determining the absolute configuration of chiral molecules and core-resonant CD is particularly well suited to gauge local molecular chirality [83]. As Eq. (37) was derived assuming complex polarization vectors, the implementation presented here can easily be used to generate spectra involving pulses with circular (or, more general, elliptical) polarization, including at short wavelengths.

As alluded to above, the leading contributions to a CD spectrum arise from the magnetic dipole and electric quadrupole terms in the multipole expansion of the vector potential. In an isotropic sample, the quadrupole contribution vanishes since the electric dipole–electric quadrupole component of the rotatory strength tensor is traceless [32]. As a prototypical example which previously has been used to test new implementations of CD spectra [84–86], we will consider the H_2O_2 molecule in a chiral conformation with fixed orientation relative to the external laser pulse.

The CD spectrum is calculated as the difference between the spectral response functions of two distinct simulations: one with left circular polarization and one with right circular polarization of the pulse. We define the normalized differential absorption as

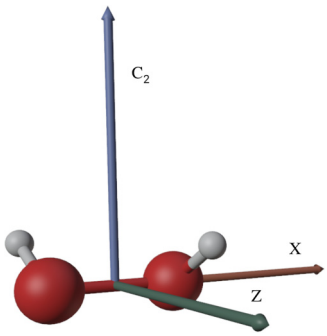

FIG. 7. Definition of the Cartesian coordinate system for H_2O_2 (C_2 point group).

$$\bar{S}_{l-r}(\omega) = \bar{S}_l(\omega) - \bar{S}_r(\omega), \tag{43}$$

where $\bar{S}_l(\omega)$ and $\bar{S}_r(\omega)$ are the normalized spectral response functions for the left and right circularly polarized pulses. The molecular geometry of H_2O_2, depicted in Fig. 7 along with the Cartesian axis definitions, is taken from Ref. [87] (see Appendix C for the Cartesian coordinates). We choose the polarization vectors such that $\boldsymbol{u}^l + \boldsymbol{u}^r = \hat{\boldsymbol{j}}$, where $\hat{\boldsymbol{j}}$ is a unit vector aligned with the C_2 axis and superscripts r and l refer to right and left circular polarization, respectively, as seen from the source. We run two pairs of simulations with the propagation direction along the x axis and along the z axis. For the propagation direction along the x axis we use $\boldsymbol{u}^r = (0, 1, \mathrm{i})$ and $\boldsymbol{u}^l = (0, 1, -\mathrm{i})$, and for the propagation direction along the z axis we use $\boldsymbol{u}^r = (-\mathrm{i}, 1, 0)$ and $\boldsymbol{u}^l = (\mathrm{i}, 1, 0)$. We use a carrier frequency in the K-edge region of oxygen, $\omega = 20$ a.u. (544.23 eV), and carrier-envelope phase $\gamma = 0$. The duration of the laser pulse is ten optical cycles and the trigonometric envelope is defined with $n = 2$, which corresponds to $\tau = 1.14$ a.u. The electric-field strength is $E_1 = 0.01$ a.u. (peak intensity 3.51×10^{12} W/cm^2) and the carrier-envelope phase is $\gamma = 0$. The time step is $\Delta t = 0.005$ a.u. and the total simulation time is 1000 a.u. We use the TDHF, TDCIS, TDCC2, TDOMP2, and TDCCSD methods with the cc-pVDZ basis set [88,89], and the spectra for propagation direction along the x and z axes are normalized with respect to the corresponding TDCIS simulation. The resulting CD spectra are plotted in Figs. 8 and 9. As in the Ti^{4+} simulations above, we see that the TDCIS and TDHF methods produce nearly identical CD spectra with minor visual differences. The TDCC2 and TDOMP2 methods also yield similar CD spectra, producing the same sign pattern of the differential absorption peaks, although the TDOMP2 peak positions are slightly more redshifted than the TDCC2 ones relative to the TDHF peaks. The intensities of the TDCC2 and TDOMP2 spectra are significantly reduced compared with the TDHF and TDCIS spectra. The TDCCSD method shifts the transition frequencies somewhat but produces an intensity of the dominant peak around 561−562 eV which is closer to that of TDHF theory than the TDCC2 and TDOMP2 methods. Although this may indicate that high-level

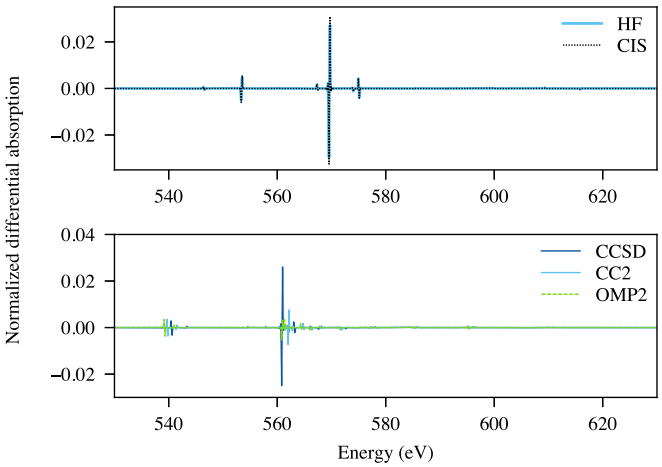

FIG. 8. Differential spectra obtained with the cc-pVDZ basis set in the K-edge region of H_2O_2 with the propagation direction along the x axis.

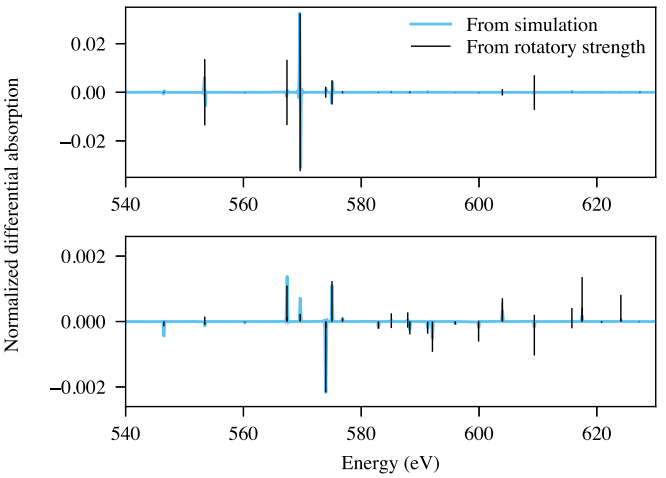

FIG. 10. Differential spectra obtained with the cc-pVDZ basis set in the K-edge region of H_2O_2 with propagation direction along the x (top) and z (bottom) axes, along with circular dichroism calculated from rotatory strengths.

electron-correlation treatment is important, the deviation may also be caused by limited frequency resolution (discussed below). Of course, the choice of carrier frequency will affect the relative peak magnitudes, but further tests have shown that this effect is rather marginal as long as ω is reasonably close to the transition energies. Figure 10 shows the CD spectrum obtained from the TDCIS simulations along with a stick spectrum calculated from the rotatory strength tensors [32] computed by full diagonalization of the CIS Hamiltonian matrix. For both propagation directions, the stick spectrum is normalized such that the maximum peak is equal to the maximum peak from the corresponding TDCIS simulation. Since the carrier frequency is 544.23 eV, it is expected that the peaks of the stick spectrum are smaller than the simulated peaks to the immediate left of the dominant peak and larger further to the right of the dominant peak. This is indeed what we observe in the bottom panel of Fig. 10. In the top panel, however, this is not the case. This can be ascribed to insufficient convergence. The excited states of H_2O_2 in the C_2 geometry

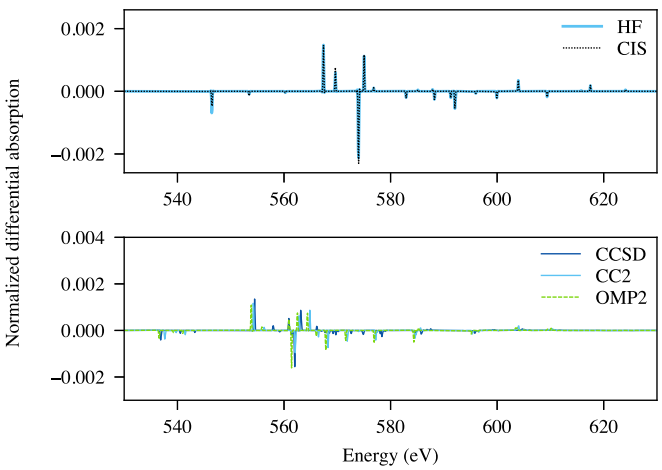

FIG. 9. Differential spectra obtained with the cc-pVDZ basis set in the K-edge region of H_2O_2 with the propagation direction along the z axis.

come in pairs, typically separated by 0.01 eV or less, formed by the lowering of symmetry relative to a planar, achiral (cis or trans) structure. For propagation in the x direction, the CDs for these pairs of states are of about the same magnitude but with opposite signs, causing lowering of the peak intensities. Figure 11 shows the effect of increasing the simulation time from 1000 a.u. to 7500 a.u. The change in the bottom panel is relatively minor, while the dominant peak in the top panel has increased by an order of magnitude. This is closer to the expected difference calculated from rotatory strength tensors. However, the peak at 567 eV is still much suppressed, which is caused by the states only being separated by about 0.0088 eV.

An overview of the occupied orbitals and the 11 lowest-lying virtual orbitals is given in Table I. The core orbitals $1\sigma_s$ and $1\sigma_s^*$ are separated by 7.3483×10^{-3} eV and

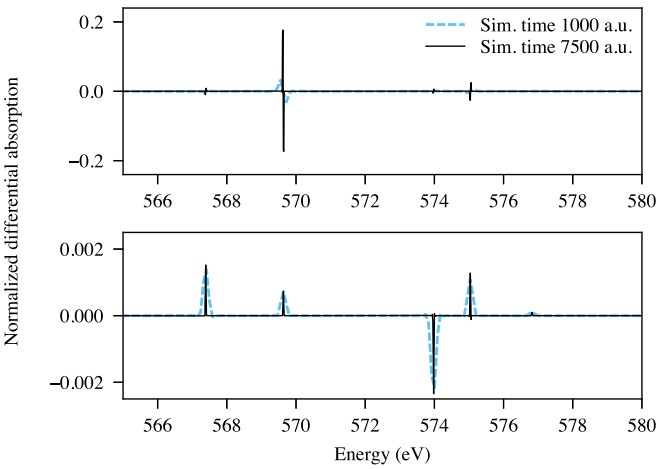

FIG. 11. TDCIS differential spectra obtained with the cc-pVDZ basis set in the K-edge region of H_2O_2 with the propagation direction along the x (top) and z (bottom) axes, with simulation times of 1000 and 7500 a.u.

TABLE I. Occupied orbitals and the 11 lowest-lying virtual orbitals of H_2O_2 with the cc-pVDZ basis set. The orbital types are based on similarity to the peroxide ion. Due to the reduced symmetry, all orbitals are somewhat mixed.

No.	Energy (a.u.)	Symmetry label	Type
1	−561.27036	1*A*	σ
2	−561.26301	1*B*	σ^*
3	−39.992527	2*A*	σ
4	−33.108905	2*B*	σ
5	−19.465831	3*B*	π_z
6	−18.833153	3*A*	π_y
7	−16.202217	4*A*	σ_{p_x}
8	−14.251659	5*A*	π_z^*
9	−13.038506	4*B*	π_y^*
10	5.1526056	6*A*	σ
11	5.2866155	5*B*	σ^*
12	7.7990137	6*B*	$\sigma_{p_x}^*$
13	22.642558	7*A*	mixed, dominant weight on H
14	22.835716	7*B*	mixed, dominant weight on H
15	30.276955	8*B*	$\sigma_{s\text{-}p_x}^*$
16	30.673602	8*A*	π_y-π_z^*
17	31.260347	9*A*	π_z^*
18	32.689754	9*B*	$\sigma_{p_x}^*$-π_y^*
19	34.770868	10*B*	mixed σ-π
20	36.906177	10*A*	$\sigma_{s\text{-}p_x}^*$

hence excitations from either of the core orbitals to low-lying virtual orbitals will fall in the K–pre-edge region. The TDCIS spectrum contains five main peaks below 580 eV along with three smaller ones at 553.44, 560.24, and 576.82 eV. The first peak at 546.48 eV can be viewed as a transition to virtual orbitals 5*B* and 6*B*. The main peak in Fig. 8 at 569.63 eV contains significant excitations to orbitals 8*A*, 9*A*, and 9*B*, which are orbitals with significant π character, and with electron density mostly located on the oxygen atoms. The main peak in Fig. 9 at 573.97 eV is mainly due to excitations to the 7*B* and 8*B* (and somewhat to 10*A*) orbitals.

Finally, noting that the cc-pVDZ basis set is insufficient for accurate predictions of CD spectra in general (see, e.g., Ref. [84]), we compare the TDCIS spectra with those obtained with larger basis sets in Fig. 12. As expected, the basis-set effect is significant. Going from a double-zeta to a triple-zeta basis retains some of the main features but the energies are red-shifted, whereas the inclusion of diffuse orbitals in the aug-cc-pVDZ basis set leads to a much more radical change of the underlying dynamics due to a higher density of excited states in the energy region around the carrier frequency. More accurate predictions of transient CD spectra, especially with the higher-level TDCC methods, clearly require larger basis sets including diffuse functions.

IV. CONCLUSION

We have derived a gauge-invariant expression for the spectral response function which is applicable to transient absorption and emission spectra. This expression is applicable

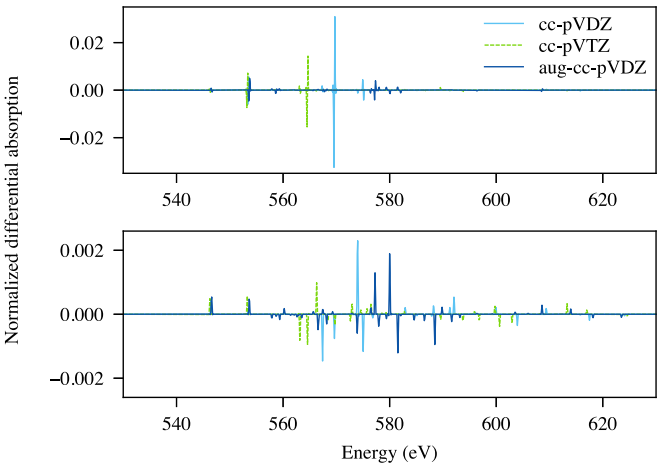

FIG. 12. TDCIS CD spectra in the K-edge region of H_2O_2 with the propagation direction along the x axis (top) and z axis (bottom).

both within and beyond the electric dipole approximation. Using an enveloped plane-wave vector potential to formulate the semiclassical matter-field interaction operator, simulations of laser-driven many-electron dynamics with a fixed atom-centered Gaussian basis set can be straightforwardly carried out with no additional cost compared with the analogous electric dipole simulations. Numerical experiments show that beyond-dipole effects are fully captured without explicit multipole expansions and that electric dipole results are correctly reproduced in the long-wavelength limit. Circular (or, more general, elliptical) polarization is easily handled, as illustrated by preliminary simulations of anisotropic transient x-ray circular dichroism spectra.

Aimed at electronic ground and bound excited states, fixed atom-centered Gaussian basis sets do not support electronic continuum states and consequently we have only considered low-intensity laser fields in this work. An extension of the approach presented here to more flexible bases would allow

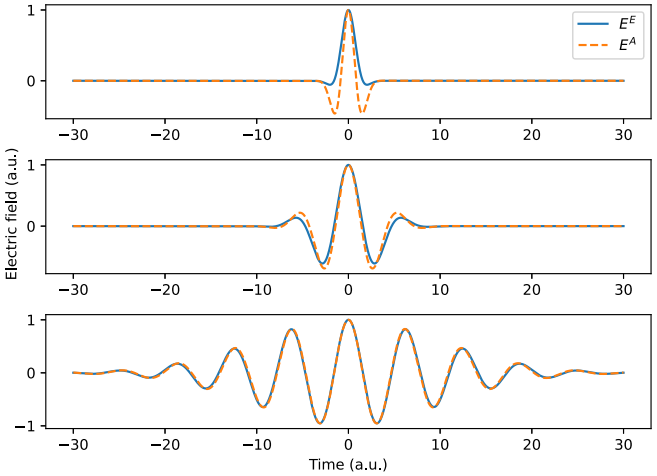

FIG. 13. Comparison of E^E (envelope on the electric field) and E^A (envelope on the vector potential). Common parameters were $\omega = 1$ and $\phi = 0$. In addition, $\sigma = 1$ (top), $\sigma = 3$ (middle), and $\sigma = 10$ (bottom).

us to study highly nonlinear processes such as core ionization where the magnetic component of the electromagnetic field may play a decisive role.

ACKNOWLEDGMENTS

This work was supported by the Research Council of Norway through its Centres of Excellence scheme, Project No. 262695. The calculations were performed on resources provided by Sigma2, the National Infrastructure for High Performance Computing and Data Storage in Norway, Grant No. NN4654K. S.K. and T.B.P. acknowledge support from the Centre for Advanced Study in Oslo, Norway. R.L. acknowledges the Swedish Research Council (VR, Grant No. 2020-03182) for funding.

APPENDIX A: WEYL QUANTIZATION OF THE CLASSICAL POWER

For notational convenience, we will consider Weyl quantization [38] in one spatial dimension; the generalization to three dimensions is straightforward. We will use (q, p) to denote a point in the classical phase space and $\hat{q}, \hat{p}$ to denote the corresponding quantum-mechanical operators satisfying the canonical commutator (using atomic units throughout)

$$[\hat{q}, \hat{p}] = \mathrm{i}. \tag{A1}$$

The classical power is given by

$$P(q, p) = [p + A(q,t)]E(q,t) = pE(q,t) + A(q,t)E(q,t). \tag{A2}$$

The second term is easily quantized since both A and E are local functions. Assuming that E is an analytic function of q, we may write

$$pE(q,t) = \sum_{s=0}^{\infty} \frac{E^{(s)}(0,t)}{s!} pq^s, \tag{A3}$$

where $E^{(s)}(0,t)$ is the sth derivative of E with respect to q evaluated at $q = 0$. Following McCoy, the quantization of pq^s is given by [37]

$$pq^s \to \frac{1}{2^s} \sum_{l=0}^{s} \binom{s}{l} \hat{q}^{s-l} \hat{p} \hat{q}^l. \tag{A4}$$

By a simple reordering of the terms, this can be equivalently written as

$$pq^s \to \frac{1}{2^s} \sum_{l=0}^{s} \binom{s}{s-l} \hat{q}^l \hat{p} \hat{q}^{s-l}. \tag{A5}$$

We now add the two equivalent quantizations of pq^s, divide by 2, and utilize

$$\binom{s}{l} = \binom{s}{s-l} \tag{A6}$$

to obtain

$$\begin{aligned} pq^s &\to \frac{1}{2^{s+1}} \sum_{l=0}^{s} \binom{s}{l} (\hat{q}^{s-l} \hat{p} \hat{q}^l + \hat{q}^l \hat{p} \hat{q}^{s-l}) \\ &= \frac{1}{2^{s+1}} \sum_{l=0}^{s} \binom{s}{l} \{\hat{q}^{s-l} (\hat{q}^l \hat{p} + [\hat{p}, \hat{q}^l]) \\ &\quad + (\hat{p}\hat{q}^l - [\hat{p}, \hat{q}^l])\hat{q}^{s-l}\} \\ &= \frac{1}{2^{s+1}} \sum_{l=0}^{s} \binom{s}{l} (\hat{q}^s \hat{p} + \hat{p}\hat{q}^s + [\hat{q}^{s-l}, [\hat{p}, \hat{q}^l]]) \\ &= \frac{1}{2^{s+1}} \sum_{l=0}^{s} \binom{s}{l} (\hat{q}^s \hat{p} + \hat{p}\hat{q}^s). \end{aligned} \tag{A7}$$

In the last step, we have used $[\hat{p}, \hat{q}^l] = -\mathrm{i}l\hat{q}^{l-1}$ to conclude that $[\hat{q}^{s-l}, [\hat{p}, \hat{q}^l]] = 0$. Using the sum rule

$$\sum_{l=0}^{s} \binom{s}{l} = 2^s, \tag{A8}$$

which is a special case of the binomial theorem [see, e.g., Eq. (3.1.6) in [90]], we get

$$pq^s \to \tfrac{1}{2}(\hat{p}\hat{q}^s + \hat{q}^s \hat{p}). \tag{A9}$$

Consequently,

$$\begin{aligned} pE(q,t) &= \sum_{s=0}^{\infty} \frac{E^{(s)}(0,t)}{s!} pq^s \\ &\to \frac{1}{2} \sum_{s=0}^{\infty} \frac{E^{(s)}(0,t)}{s!} (\hat{p}\hat{q}^s + \hat{q}^s \hat{p}) \\ &= \frac{1}{2}[\hat{p}E(\hat{q},t) + E(\hat{q},t)\hat{p}], \end{aligned} \tag{A10}$$

and the power operator thus becomes

$$P(q,p) \to \tfrac{1}{2}[\hat{\pi}E(\hat{q},t) + E(\hat{q},t)\hat{\pi}], \tag{A11}$$

where $\hat{\pi} = \hat{p} + A(\hat{q}, t)$.

APPENDIX B: GAUGE INVARIANCE OF THE ENERGY OPERATOR

We consider the gauge transformation

$$\boldsymbol{A}'(\boldsymbol{r},t) = \boldsymbol{A}(\boldsymbol{r},t) + \nabla\chi(\boldsymbol{r},t), \tag{B1}$$

$$\phi'(\boldsymbol{r},t) = \phi(\boldsymbol{r},t) - \frac{\partial\chi(\boldsymbol{r},t)}{\partial t}, \tag{B2}$$

where $\boldsymbol{A}$ and ϕ are the vector and scalar potentials in gauge g, and $\boldsymbol{A}'$ and ϕ' are the corresponding potentials in gauge g'. The gauge function χ is an arbitrary (differentiable) function. Starting with the Schrödinger equation in gauge g,

$$\mathrm{i}|\dot{\Psi}_g\rangle = H(\boldsymbol{A}, \phi)|\Psi_g\rangle, \tag{B3}$$

where the overdot denotes the time derivative and $H(\boldsymbol{A}, \phi) = \frac{1}{2}(\boldsymbol{p} + \boldsymbol{A})^2 + W - \phi$, the corresponding state in gauge g',

$$|\Psi_{g'}\rangle = U|\Psi_g\rangle = \mathrm{e}^{-\mathrm{i}\chi}|\Psi_g\rangle, \tag{B4}$$

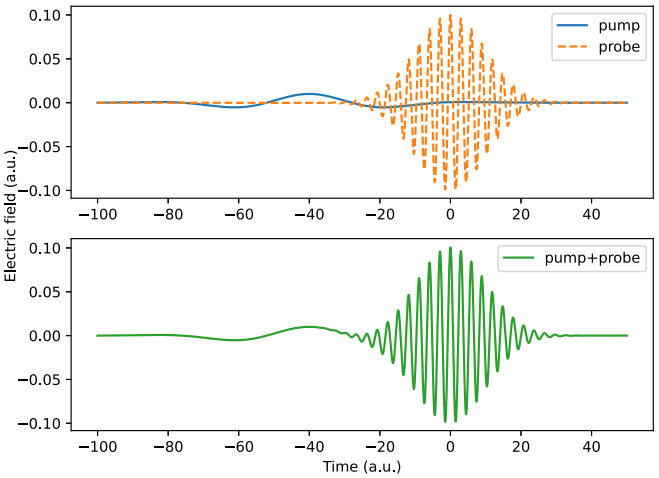

FIG. 14. Illustration of the electric field of the LiH pump-probe simulations using E^E.

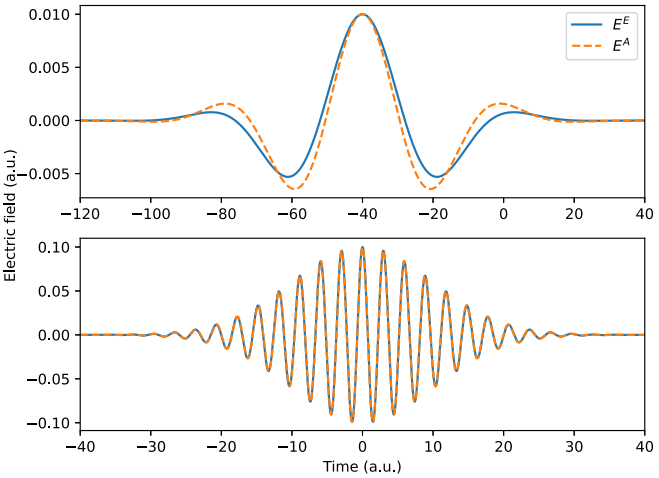

FIG. 15. Comparison of the pump and probe pulses using E^E and E^A pulses.

satisfies the Schrödinger equation

$$\mathrm{i}|\dot{\Psi}_{g'}\rangle = H(\boldsymbol{A}', \phi')|\Psi_{g'}\rangle. \tag{B5}$$

The two Hamiltonians are related by

$$H(\boldsymbol{A}', \phi') = UH(\boldsymbol{A}, \phi)U^\dagger + \mathrm{i}\dot{U}U^\dagger, \tag{B6}$$

and therefore the expectation values of the Hamiltonian in the two gauges are not equivalent:

$$\begin{aligned}
&\langle\Psi_{g'}|H(\boldsymbol{A}', \phi')|\Psi_{g'}\rangle \\
&\quad = \langle\Psi_g|U^\dagger[UH(\boldsymbol{A}, \phi)U^\dagger + \mathrm{i}\dot{U}U^\dagger]U|\Psi_g\rangle \\
&\quad = \langle\Psi_g|H(\boldsymbol{A}, \phi)|\Psi_g\rangle + \mathrm{i}\langle\Psi_g|U^\dagger\dot{U}|\Psi_g\rangle \\
&\quad = \langle\Psi_g|H(\boldsymbol{A}, \phi)|\Psi_g\rangle + \langle\Psi_g|\dot{\chi}|\Psi_g\rangle \\
&\quad = \langle\Psi_g|H(\boldsymbol{A}, \phi)|\Psi_g\rangle + \langle\Psi_g|\phi - \phi'|\Psi_g\rangle.
\end{aligned} \tag{B7}$$

This explicitly shows that the Hamiltonian does *not* represent the energy of the electrons in the presence of external time-dependent electromagnetic fields. However, a simple rearrangement of this expression yields

$$\langle\Psi_{g'}|H(\boldsymbol{A}', \phi') + \phi'|\Psi_{g'}\rangle = \langle\Psi_g|H(\boldsymbol{A}, \phi) + \phi|\Psi_g\rangle, \tag{B8}$$

which indicates that a gauge-invariant energy operator can be defined as $H(\boldsymbol{A}, \phi) + \phi$.

An operator $F(\boldsymbol{A}, \phi)$ has gauge-invariant expectation values if the change in vector and scalar potentials induces a change in the operator such that

$$F(\boldsymbol{A}', \phi') = UF(\boldsymbol{A}, \phi)U^\dagger. \tag{B9}$$

In this case,

$$\langle\Psi_g|F(\boldsymbol{A}, \phi)|\Psi_g\rangle = \langle\Psi_{g'}|F(\boldsymbol{A}', \phi')|\Psi_{g'}\rangle. \tag{B10}$$

Under a gauge transformation, the energy operator [40,41]

$$K(\boldsymbol{A}) = H(\boldsymbol{A}, \phi) + \phi = \tfrac{1}{2}\pi^2 + W \tag{B11}$$

transforms as

$$\begin{aligned}
UK(\boldsymbol{A})U^\dagger &= \tfrac{1}{2}U(\boldsymbol{p} + \boldsymbol{A})^2U^\dagger + W \\
&= \tfrac{1}{2}(\boldsymbol{p} + \boldsymbol{A}')^2 + W \\
&= K(\boldsymbol{A}').
\end{aligned} \tag{B12}$$

We can thus conclude that the expectation value of the energy operator is indeed gauge invariant.

The energy operator can be reduced to the field-free operator $H_0 = \frac{p^2}{2} + W$ by a gauge transformation if and only if there is no magnetic field present, $\nabla \times \boldsymbol{A} = 0$. Within the electric dipole approximation, this gauge choice gives the dipole-length Hamiltonian. Beyond the electric dipole approximation, however, no such gauge choice exists.

Although one may always expand the wave function in the eigenstates of H_0 (with a suitable representation of the continuous part of the spectrum), the expansion coefficients

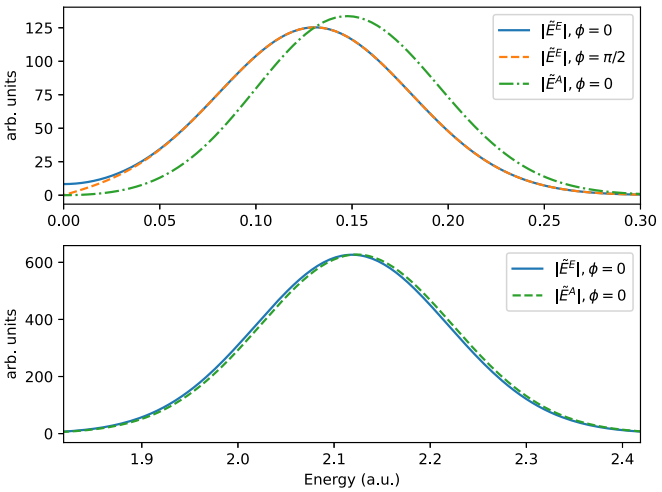

FIG. 16. Magnitude of the Fourier components in the pump (top) and probe (bottom) pulses using the E^A pulse and E^E pulses with carrier-envelope phase 0 and $\pi/2$.

TABLE II. Cartesian coordinates in bohrs.

		LiH	
Li	0.0	0.0	0.0
H	0.0	0.0	−3.0139491027559635
		$TiCl_4$	
Ti	0.0	0.0	0.0
Cl	0.0	0.0	4.1007056904379215
Cl	3.86618240181189	0.0	−1.3669018968126405
Cl	−1.93309120090594	3.348212175633433	−1.3669018968126405
Cl	−1.93309120090594	−3.348212175633433	−1.3669018968126405
		H_2O_2	
O	1.3936730169115057	0.0	0.0
O	−1.3936730169115057	0.0	0.0
H	1.5439062438192541	0.8972419639723157	1.5476856960685057
H	−1.5439062438192541	0.8972419639723157	−1.5476856960685057

are gauge dependent and hence cannot be interpreted as transition amplitudes. Gauge-independent expansion coefficients are only obtained if the proper energy states, i.e., the instantaneous eigenstates of the energy operator, are used [40].

APPENDIX C: MOLECULAR GEOMETRIES

The nuclear Cartesian coordinates in Bohr for the molecules studied in the main text are listed in Table II.

APPENDIX D: PULSE SHAPES AND FREQUENCY COMPONENTS

1. Definitions of pulses

Electric-field pulse shapes of the form

$$\begin{aligned}\boldsymbol{E}^E(t) &= \sum_{n=1}^{N} \boldsymbol{E}_n^E(t) \\ &= \sum_{n=1}^{N} E_n \boldsymbol{u}_n \cos[\omega_n(t-t_n)-\phi_n] G_n(t) \end{aligned} \tag{D1}$$

are common in the literature [usually in singular form $\boldsymbol{E}^E(t) = \boldsymbol{E}_1^E(t)$]. In Eq. (D1), n is the pulse number, N is the number of pulses, E_n is the maximum field strength, $\boldsymbol{u}_n$ is a real polarization vector, ω_n is the carrier frequency, t_n is the central time, $G_n(t)$ is the envelope, and ϕ_n is the carrier-envelope phase. Superscript E signifies that the envelope has been placed on the electric field. Here we will use Gaussian envelopes defined by

$$G_n(t) = \exp\left(\frac{-(t-t_n)^2}{2\sigma_n^2}\right), \tag{D2}$$

where σ_n is the standard deviation. Alternatively, we can define the electric field by the vector potential in velocity gauge, $\boldsymbol{E}(t) = -\partial_t \boldsymbol{A}(t)$, where we define the vector potential as

$$\boldsymbol{A}(t) = -\sum_{n=1}^{N} A_n \boldsymbol{u}_n \sin[\omega_n(t-t_n)-\phi_n] G_n(t). \tag{D3}$$

The corresponding electric field is then

$$\begin{aligned}\boldsymbol{E}^A(t) &= \sum_{n=1}^{N} \boldsymbol{E}_n^A(t) \\ &= \sum_{n=1}^{N} E_n \boldsymbol{u}_n \Big(\cos[\omega_n(t-t_n)-\phi_n] \\ &\quad - \frac{t-t_n}{\omega_n \sigma_n^2} \sin[\omega_n(t-t_n)-\phi_n] \Big) G_n(t), \end{aligned} \tag{D4}$$

where superscript A denotes that the envelope was placed on the vector potential and $E_n = \omega_n A_n$. For a given carrier frequency ω_n, $E_n^A(t)$ will converge to $E_n^E(t)$ for increasing values of σ_n, but in cases where σ_n is small in the sense that we have effectively few cycles, $E_n^A(t)$ may differ significantly from $E_n^E(t)$. An illustration of this is shown in Fig. 13.

2. Frequency components

The zero-frequency (dc) component of the electric field is given by

$$\tilde{\boldsymbol{E}}(0) = \int_{-\infty}^{\infty} \boldsymbol{E}(t) dt. \tag{D5}$$

The dc component should vanish in the far-field approximation of the Maxwell equations [50]. This condition is by definition satisfied by the pulse given in Eq. (D4). It is in general not satisfied for pulses defined by Eq. (D1), but the dc component will vanish for phases $\phi_n = (m + \frac{1}{2})\pi$, $m \in \mathbb{Z}$, since the function is then odd. In what follows, we use the

TABLE III. Parameters used in pump-probe setup. All values are in atomic units.

Parameter	Pump	Probe
E_n	0.01	0.1
ω_n	0.130551	2.118698
ϕ_n	0	0
σ_n	20	10
t_n	−40	0

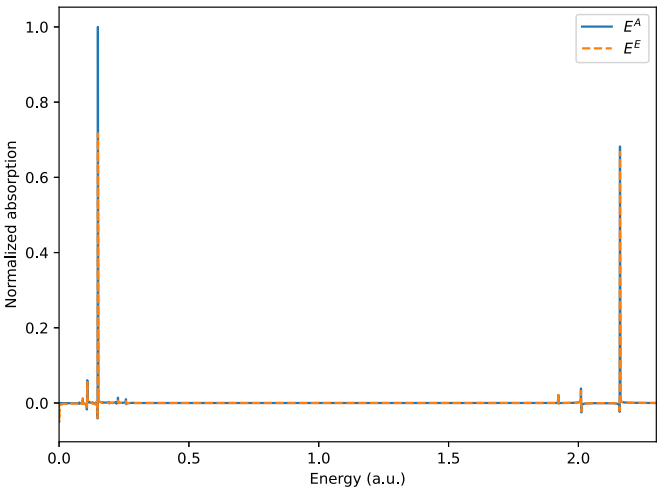

FIG. 17. Transient spectrum using the E^A and E^E pulses.

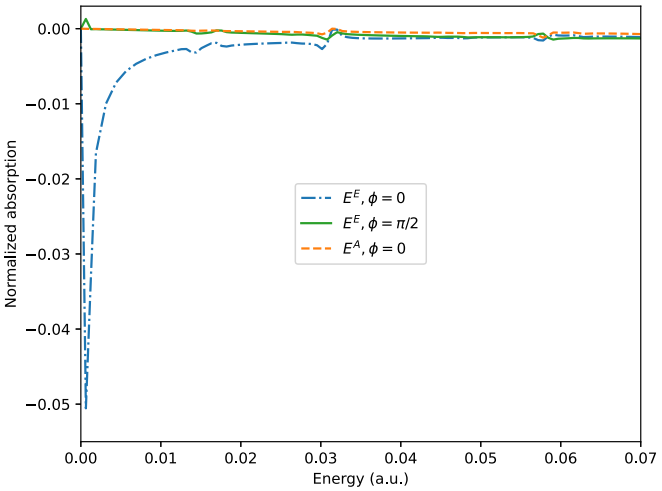

FIG. 18. Zero-frequency region of the transient spectrum using the E^A pulse and E^E pulses with carrier-envelope phase 0 and $\pi/2$.

magnitude of the Fourier component defined as

$$|\tilde{f}(\omega)| = \left| \int_{\infty}^{\infty} f(t) e^{-i\omega t} dt \right| \tag{D6}$$

to analyze the frequency components in the pulses.

3. Example: LiH pump-probe pulse

We will here look at the pump-probe pulse used for LiH in Ref. [34], where the electric field was of the form given in Eq. (D1) and polarized in the z direction. An illustration of the pulses is given in Fig. 14. The parameters are given in Table III.

Here we will refer to these generally as E^E pulses, as opposed to the corresponding pulses generated with Eq. (D4) using the same parameters, which we will refer to as E^A pulses. A comparison between the E^E and E^A pump and probe pulses is shown in Fig. 15. As expected, the difference between the probe pulses is quite small since they have (relatively) many cycles, while the difference between the pump pulses is quite significant since they have few cycles.

Figure 16 shows the magnitude of Fourier components of the E^E and E^A pulses. In the figure, an E^E pump pulse with $\phi = \pi/2$ has also been included. We note that $|\tilde{E}^E(\omega_n)|$ and $|\tilde{E}^A(\omega_n)|$ are similar, but the central frequencies of the E^A pulses are higher and have larger maximum Fourier components. Expectedly, these differences are quite large for the pump pulses and much smaller for the probe pulses. Also, we see (as mentioned above) that the E^E pulse with $\phi = 0$ has a nonvanishing zero-frequency component.

Figure 17 shows a comparison between a pump-probe spectrum generated with the E^E and corresponding E^A pulses using TDRCIS. We see that the spectra show very small deviations in the probe region, while the difference in absorption in the pump region is large, in accordance with the preceding analysis.

We can also note that the E^E spectrum has an unphysical close-to-zero-frequency component. This is also visible in Fig. 1 in Ref. [34]. Figure 18 shows this in in more detail and also includes an E^E spectrum with $\phi_1 = \phi_2 = \pi/2$. The zero-frequency component is practically gone in the spectra generated from electric fields with zero dc component, and it is therefore natural to connect this to the nonvanishing dc component of the electric field.

[1] P. B. Corkum and F. Krausz, Attosecond science, Nat. Phys. **3**, 381 (2007).

[2] F. Krausz and M. Ivanov, Attosecond physics, Rev. Mod. Phys. **81**, 163 (2009).

[3] M. Nisoli, P. Decleva, F. Calegari, A. Palacios, and F. Martín, Attosecond electron dynamics in molecules, Chem. Rev. **117**, 10760 (2017).

[4] M. Klinker, C. Marante, L. Argenti, J. González-Vázquez, and F. Martín, Electron correlation in the ionization continuum of molecules: Photoionization of N_2 in the vicinity of the Hopfield series of autoionizing states, J. Phys. Chem. Lett. **9**, 756 (2018).

[5] K. C. Kulander, Time-dependent theory of multiphoton ionization of xenon, Phys. Rev. A **38**, 778 (1988).

[6] K. J. Schafer and K. C. Kulander, Energy analysis of time-dependent wave functions: Application to above-threshold ionization, Phys. Rev. A **42**, 5794 (1990).

[7] K. C. Kulander, K. J. Schafer, and J. L. Krause, in *Super-Intense Laser-Atom Physics*, edited by B. Piraux, A. L'Huillier, and K. Rzążewski, NATO Advanced Studies Institute, Series B: Physics, Vol. 316 (Springer, Boston, 1993), pp. 95–110.

[8] M. Lezius, V. Blanchet, D. M. Rayner, D. M. Villeneuve, A. Stolow, and M. Y. Ivanov, Nonadiabatic multielectron dynamics in strong field molecular ionization, Phys. Rev. Lett. **86**, 51 (2001).

[9] A. N. Markevitch, S. M. Smith, D. A. Romanov, H. B. Schlegel, M. Y. Ivanov, and R. J. Levis, Nonadiabatic dynamics of polyatomic molecules and ions in strong laser fields, Phys. Rev. A **68**, 011402(R) (2003).

[10] J. Olsen and P. Jørgensen, Linear and nonlinear response functions for an exact state and for an MCSCF state, J. Chem. Phys. **82**, 3235 (1985).

[11] N. H. List, J. Kauczor, T. Saue, H. J. A. Jensen, and P. Norman, Beyond the electric-dipole approximation: A formulation and implementation of molecular response theory for the description of absorption of electromagnetic field radiation, J. Chem. Phys. **142**, 244111 (2015).

[12] N. H. List, T. Saue, and P. Norman, Rotationally averaged linear absorption spectra beyond the electric-dipole approximation, Mol. Phys. **115**, 63 (2017).

[13] L. K. Sørensen, E. Kieri, S. Srivastav, M. Lundberg, and R. Lindh, Implementation of a semiclassical light-matter interaction using the Gauss-Hermite quadrature: A simple alternative to the multipole expansion, Phys. Rev. A **99**, 013419 (2019).

[14] M. van Horn, T. Saue, and N. H. List, Probing chirality across the electromagnetic spectrum with the full semi-classical light–matter interaction, J. Chem. Phys. **156**, 054113 (2022).

[15] S. Bernadotte, A. J. Atkins, and C. R. Jacob, Origin-independent calculation of quadrupole intensities in X-ray spectroscopy, J. Chem. Phys. **137**, 204106 (2012).

[16] P. J. Lestrange, F. Egidi, and X. Li, The consequences of improperly describing oscillator strengths beyond the electric dipole approximation, J. Chem. Phys. **143**, 234103 (2015).

[17] L. K. Sørensen, R. Lindh, and M. Lundberg, Gauge origin independence in finite basis sets and perturbation theory, Chem. Phys. Lett. **683**, 536 (2017).

[18] M. van Horn, N. H. List, and T. Saue, Transition moments beyond the electric-dipole approximation: Visualization and basis set requirements, J. Chem. Phys. **158**, 184103 (2023).

[19] M. Wu, S. Chen, S. Camp, K. J. Schafer, and M. B. Gaarde, Theory of strong-field attosecond transient absorption, J. Phys. B **49**, 062003 (2016).

[20] N. Rohringer, A. Gordon, and R. Santra, Configuration-interaction-based time-dependent orbital approach for *ab initio* treatment of electronic dynamics in a strong optical laser field, Phys. Rev. A **74**, 043420 (2006).

[21] P. Krause, T. Klamroth, and P. Saalfrank, Molecular response properties from explicitly time-dependent configuration interaction methods, J. Chem. Phys. **127**, 034107 (2007).

[22] H. B. Schlegel, S. M. Smith, and X. Li, Electronic optical response of molecules in intense fields: Comparison of TD-HF, TD-CIS, and TD-CIS(D) approaches, J. Chem. Phys. **126**, 244110 (2007).

[23] S. Pabst, L. Greenman, P. J. Ho, D. A. Mazziotti, and R. Santra, Decoherence in attosecond photoionization, Phys. Rev. Lett. **106**, 053003 (2011).

[24] A. F. White, C. J. Heide, P. Saalfrank, M. Head-Gordon, and E. Luppi, Computation of high-harmonic generation spectra of the hydrogen molecule using time-dependent configuration-interaction, Mol. Phys. **114**, 947 (2016).

[25] B. S. Ofstad, E. Aurbakken, Ø. S. Schøyen, H. E. Kristiansen, S. Kvaal, and T. B. Pedersen, Time-dependent coupled-cluster theory, WIREs Comput. Mol. Sci. **13**, e1666 (2023).

[26] O. Kfir, P. Grychtol, E. Turgut, R. Knut, D. Zusin, D. Popmintchev, T. Popmintchev, H. Nembach, J. M. Shaw, A. Fleischer, H. Kapteyn, M. Murnane, and O. Cohen, Generation of bright phase-matched circularly-polarized extreme ultraviolet high harmonics, Nat. Photon. **9**, 99 (2015).

[27] A. D. Bandrauk and K.-J. Yuan, Circularly polarised attosecond pulses: Generation and applications, Mol. Phys. **114**, 344 (2016).

[28] R. Shao, C. Zhai, Y. Zhang, N. Sun, W. Cao, P. Lan, and P. Lu, Generation of isolated circularly polarized attosecond pulses by three-color laser field mixing, Opt. Express **28**, 15874 (2020).

[29] G. Ma, W. Yu, M. Y. Yu, B. Shen, and L. Veisz, Intense circularly polarized attosecond pulse generation from relativistic laser plasmas using few-cycle laser pulses, Opt. Express **24**, 10057 (2016).

[30] C. Zhong, B. Qiao, Y. Zhang, Y. Zhang, X. Li, J. Wang, C. Zhou, S. Zhu, and X. He, Production of intense isolated attosecond pulses with circular polarization by using counter-propagating relativistic lasers, New J. Phys. **23**, 063080 (2021).

[31] C. Chen, Z. Tao, C. Hernández-García, P. Matyba, A. Carr, R. Knut, O. Kfir, D. Zusin, C. Gentry, P. Grychtol, O. Cohen, L. Plaja, A. Becker, A. Jaron-Becker, H. Kapteyn, and M. Murnane, Tomographic reconstruction of circularly polarized high-harmonic fields: 3D attosecond metrology, Sci. Adv. **2**, e1501333 (2016).

[32] T. B. Pedersen and A. E. Hansen, *Ab initio* calculation and display of the rotatory strength tensor in the random phase approximation: Method and model studies, Chem. Phys. Lett. **246**, 1 (1995).

[33] D. J. Tannor, *Introduction to Quantum Mechanics: A Time-Dependent Perspective* (University Science Books, Sausalito, 2007).

[34] A. S. Skeidsvoll, A. Balbi, and H. Koch, Time-dependent coupled-cluster theory for ultrafast transient-absorption spectroscopy, Phys. Rev. A **102**, 023115 (2020).

[35] A. Guandalini, C. Cocchi, S. Pittalis, A. Ruini, and C. A. Rozzi, Nonlinear light absorption in many-electron systems excited by an instantaneous electric field: A non-perturbative approach, Phys. Chem. Chem. Phys. **23**, 10059 (2021).

[36] J. D. Jackson, *Classical Electrodynamics*, 2nd ed. (Wiley, New York, 1975).

[37] N. H. McCoy, On the function in quantum mechanics which corresponds to a given function in classical mechanics, Proc. Natl. Acad. Sci. USA **18**, 674 (1932).

[38] H. Weyl, Quantenmechanik und gruppentheorie, Z. Phys. **46**, 1 (1927).

[39] H. Goldstein, *Classical Mechanics*, 2nd ed. (Addison-Wesley, Reading, 1980).

[40] K.-H. Yang, Gauge transformations and quantum mechanics I. Gauge invariant interpretation of quantum mechanics, Ann. Phys. (NY) **101**, 62 (1976).

[41] D. H. Kobe and K.-H. Yang, Energy of a classical charged particle in an external electromagnetic field, Eur. J. Phys. **8**, 236 (1987).

[42] K.-H. Yang, Gauge transformations and quantum mechanics II. Physical interpretation of classical gauge transformations, Ann. Phys. (NY) **101**, 97 (1976).

[43] D. H. Kobe and A. L. Smirl, Gauge invariant formulation of the interaction of electromagnetic radiation and matter, Am. J. Phys. **46**, 624 (1978).

[44] D. H. Kobe, Implications of gauge invariance for length versus velocity forms of the interaction with electric dipole radiation, Int. J. Quantum Chem. **14**, 73 (1978).
[45] D. H. Kobe and K.-H. Yang, Gauge-invariant non-relativistic limit of an electron in a time-dependent electromagnetic field, J. Phys. A: Math. Gen. **13**, 3171 (1980).
[46] Y. Aharonov and C. K. Au, The question of gauge dependence of transition probabilities in quantum mechanics: Facts, myths and misunderstandings, Phys. Lett. **86A**, 269 (1981).
[47] D. H. Kobe and E. C. T. Wen, Gauge invariance in quantum mechanics: Charged harmonic oscillator in an electromagnetic field, J. Phys. A: Math. Gen. **15**, 787 (1982).
[48] R. R. Schlicher, W. Becker, J. Bergou, and M. O. Scully, in *Quantum Electrodynamics and Quantum Optics*, edited by A. O. Barut, NATO Advanced Studies Institute, Series B: Physics, Vol. 110 (Springer, Boston, 1984), pp. 405–441.
[49] I. Barth and C. Lasser, Trigonometric pulse envelopes for laser-induced quantum dynamics, J. Phys. B **42**, 235101 (2009).
[50] J. Rauch and G. Mourou, The time integrated far field for Maxwell's and D'Alembert's equations, Proc. Am. Math. Soc. **134**, 851 (2006).
[51] M. Førre, S. Selstø, J. P. Hansen, and L. B. Madsen, Exact nondipole Kramers-Henneberger form of the light-atom Hamiltonian: An application to atomic stabilization and photoelectron energy spectra, Phys. Rev. Lett. **95**, 043601 (2005).
[52] M. Førre, J. P. Hansen, L. Kocbach, S. Selstø, and L. B. Madsen, Nondipole ionization dynamics of atoms in superintense high-frequency attosecond pulses, Phys. Rev. Lett. **97**, 043601 (2006).
[53] T. E. Moe and M. Førre, Ionization of atomic hydrogen by an intense x-ray laser pulse: An *ab initio* study of the breakdown of the dipole approximation, Phys. Rev. A **97**, 013415 (2018).
[54] E. Aurbakken, K. H. Fredly, H. E. Kristiansen, S. Kvaal, R. H. Myhre, B. S. Ofstad, T. B. Pedersen, Ø. S. Schøyen, H. Sutterud, and S. G. Winther-Larsen, HyQD: Hylleraas Quantum Dynamics, available at https://github.com/HyQD.
[55] X. Li, N. Govind, C. Isborn, A. E. DePrince III, and K. Lopata, Real-time time-dependent electronic structure theory, Chem. Rev. **120**, 9951 (2020).
[56] O. Christiansen, H. Koch, and P. Jørgensen, The second-order approximate coupled cluster singles and doubles model CC2, Chem. Phys. Lett. **243**, 409 (1995).
[57] H. E. Kristiansen, B. S. Ofstad, E. Hauge, E. Aurbakken, Ø. S. Schøyen, S. Kvaal, and T. B. Pedersen, Linear and nonlinear optical properties from TDOMP2 theory, J. Chem. Theory Comput. **18**, 3687 (2022).
[58] T. B. Pedersen and S. Kvaal, Symplectic integration and physical interpretation of time-dependent coupled-cluster theory, J. Chem. Phys. **150**, 144106 (2019).
[59] H. Pathak, T. Sato, and K. L. Ishikawa, Time-dependent optimized coupled-cluster method for multielectron dynamics. II. A coupled electron-pair approximation, J. Chem. Phys. **152**, 124115 (2020).
[60] S. Kvaal, *Ab initio* quantum dynamics using coupled-cluster, J. Chem. Phys. **136**, 194109 (2012).
[61] T. B. Pedersen and H. Koch, Coupled cluster response functions revisited, J. Chem. Phys. **106**, 8059 (1997).
[62] T. B. Pedersen and H. Koch, Gauge invariance of the coupled cluster oscillator strength, Chem. Phys. Lett. **293**, 251 (1998).
[63] T. B. Pedersen, H. Koch, and C. Hättig, Gauge invariant coupled cluster response theory, J. Chem. Phys. **110**, 8318 (1999).
[64] T. B. Pedersen, B. Fernández, and H. Koch, Gauge invariant coupled cluster response theory using optimized nonorthogonal orbitals, J. Chem. Phys. **114**, 6983 (2001).
[65] T. Sato, H. Pathak, Y. Orimo, and K. L. Ishikawa, Communication: Time-dependent optimized coupled-cluster method for multielectron dynamics, J. Chem. Phys. **148**, 051101 (2018).
[66] I. Fdez. Galván, M. Vacher, A. Alavi, C. Angeli, F. Aquilante, J. Autschbach, J. J. Bao, S. I. Bokarev, N. A. Bogdanov, R. K. Carlson, L. F. Chibotaru, J. Creutzberg, N. Dattani, M. G. Delcey, S. S. Dong, A. Dreuw, L. Freitag, L. M. Frutos, L. Gagliardi, F. Gendron *et al.*, OpenMolcas: From source code to insight, J. Chem. Theory Comput. **15**, 5925 (2019).
[67] F. Aquilante, J. Autschbach, A. Baiardi, S. Battaglia, V. A. Borin, L. F. Chibotaru, I. Conti, L. De Vico, M. Delcey, I. Fdez. Galván, N. Ferré, L. Freitag, M. Garavelli, X. Gong, S. Knecht, E. D. Larsson, R. Lindh, M. Lundberg, P. Å. Malmqvist, A. Nenov *et al.*, Modern quantum chemistry with [Open]Molcas, J. Chem. Phys. **152**, 214117 (2020).
[68] J. M. H. Olsen, S. Reine, O. Vahtras, E. Kjellgren, P. Reinholdt, K. O. H. Dundas, X. Li, J. Cukras, M. Ringholm, E. D. Hedegård, R. Di Remigio, N. H. List, R. Faber, B. N. C. Tenorio, R. Bast, T. B. Pedersen, Z. Rinkevicius, S. P. A. Sauer, K. V. Mikkelsen, J. Kongsted *et al.*, Dalton Project: A Python platform for molecular- and electronic-structure simulations of complex systems, J. Chem. Phys. **152**, 214115 (2020).
[69] Q. Sun, T. C. Berkelbach, N. S. Blunt, G. H. Booth, S. Guo, Z. Li, J. Liu, J. D. McClain, E. R. Sayfutyarova, S. Sharma, S. Wouters, and G. K. Chan, PySCF: The Python-based simulations of chemistry framework, WIREs Comput. Mol. Sci. **8**, e1340 (2018).
[70] K. Aidas, C. Angeli, K. L. Bak, V. Bakken, R. Bast, L. Boman, O. Christiansen, R. Cimiraglia, S. Coriani, P. Dahle, E. K. Dalskov, U. Ekström, T. Enevoldsen, J. J. Eriksen, P. Ettenhuber, B. Fernández, L. Ferrighi, H. Fliegl, L. Frediani, K. Hald *et al.*, The Dalton quantum chemistry program system, WIREs Comput. Mol. Sci. **4**, 269 (2014).
[71] B. P. Pritchard, D. Altarawy, B. Didier, T. D. Gibsom, and T. L. Windus, A new basis set exchange: An open, up-to-date resource for the molecular sciences community, J. Chem. Inf. Model. **59**, 4814 (2019).
[72] E. Hairer, C. Lubich, and G. Wanner, *Geometric Numerical Integration*, 2nd ed. (Springer, Berlin, 2006).
[73] B. Cordero, V. Gómez, A. E. Platero-Prats, M. Revés, J. Echeverría, E. Cremades, F. Barragán, and S. Alvarez, Covalent radii revisited, Dalton Trans. **21**, 2832 (2008).
[74] S. DeBeer George, P. Brant, and E. I. Solomon, Metal and ligand K-edge XAS of organotitanium complexes: Metal 4p and 3d contributions to pre-edge intensity and their contributions to bonding, J. Am. Chem. Soc. **127**, 667 (2005).
[75] Y. C. Park, A. Perera, and R. J. Bartlett, Equation of motion coupled-cluster study of core excitation spectra II: Beyond the dipole approximation, J. Chem. Phys. **155**, 094103 (2021).
[76] L. K. Sørensen, M. Guo, R. Lindh, and M. Lundberg, Applications to metal K pre-edges of transition metal dimers illustrate the approximate origin independence for the intensities in the length representation, Mol. Phys. **115**, 174 (2017).

[77] M. Khamesian, I. Galván, M. G. Delcey, L. K. Sørensen, and R. Lindh, in *Annual Reports in Computational Chemistry*, edited by D. A. Dixon (Elsevier, Amsterdam, 2019), Vol. 15, pp. 39–76.

[78] B. O. Roos, R. Lindh, P.-Å. Malmqvist, V. Veryazov, and P.-O. Widmark, New relativistic ANO basis sets for transition metal atoms, J. Phys. Chem. A **109**, 6575 (2005).

[79] L. Rosenfeld, Quantenmechanische theorie der natürlichen optischen aktivität von flüssigkeiten und gasen, Z. Phys. **52**, 161 (1929).

[80] L. D. Barron, *Molecular Light Scattering and Optical Activity*, 2nd ed. (Cambridge University Press, Cambridge, 2004).

[81] M. Pecul and K. Ruud, in *Advances in Quantum Chemistry*, edited by H. J. Å. Jensen (Academic, New York, 2005), Vol. 50, pp. 185–212.

[82] T. D. Crawford, *Ab initio* calculation of molecular chiroptical properties, Theor. Chem. Acc. **115**, 227 (2006).

[83] Y. Zhang, J. R. Rouxel, J. Autschbach, N. Govind, and S. Mukamel, X-ray circular dichroism signals: A unique probe of local molecular chirality, Chem. Sci. **8**, 5969 (2017).

[84] A. Rizzo, B. Jansík, T. B. Pedersen, and H. Ågren, Origin invariant approaches to the calculation of two-photon circular dichroism, J. Chem. Phys. **125**, 064113 (2006).

[85] D. H. Friese and K. Ruud, Three-photon circular dichroism: Towards a generalization of chiroptical non-linear light absorption, Phys. Chem. Chem. Phys. **18**, 4174 (2016).

[86] M. Scott, D. R. Rehn, S. Coriani, P. Norman, and A. Dreuw, Electronic circular dichroism spectra using the algebraic diagrammatic construction schemes of the polarization propagator up to third order, J. Chem. Phys. **154**, 064107 (2021).

[87] R. L. Redington, W. B. Olson, and P. C. Cross, Studies of hydrogen peroxide: The infrared spectrum and the internal rotation problem, J. Chem. Phys. **36**, 1311 (1962).

[88] T. H. Dunning, Gaussian basis sets for use in correlated molecular calculations. I. The atoms boron through neon and hydrogen, J. Chem. Phys. **90**, 1007 (1989).

[89] D. E. Woon and T. H. Dunning, Gaussian basis sets for use in correlated molecular calculations. III. The atoms aluminum through argon, J. Chem. Phys. **98**, 1358 (1993).

[90] M. Abramowitz, in *Handbook of Mathematical Functions*, 10th ed., edited by M. Abramowitz and I. A. Stegun (National Bureau of Standards, Washington, DC, 1972), pp. 9–23.